A discrete-based multi-scale modeling approach for the propagation of seismic waves in soils

Tarek Mohamed, Jérôme Duriez, Guillaume Veylon, Laurent Peyras, Patrick Soulat

A discrete-based multi-scale modeling approach for the propagation of seismic waves in soils

T. Mohamed[a], J. Duriez[a,*], G. Veylon[a], L. Peyras[a], P. Soulat[b]

[a] *INRAE, Aix Marseille Univ, RECOVER, Aix-en-Provence, France*
[b] *Suez Consulting, Safege, Montpellier, France*

Abstract

A three-dimensional multi-scale discrete-continuum model (Finite Volume Method $\times$ Discrete Element Method, FVM$\times$DEM) is developed for a discrete-based description of the mechanical behavior of granular soils in boundary value problems (BVPs). In such a scheme, the constitutive response of the material is derived through direct DEM computations on a representative volume element attached to each mesh element. The developed multi-scale approach includes the inertial effect in the stress homogenization formulation and serves to study the mechanism of propagation of seismic waves, in comparison with a more classical BVP simulation that adopts an advanced bounding surface plasticity model "P2PSand". We start with a detailed and fair calibration and validation of these two models against laboratory tests for Toyoura sand under monotonic and cyclic loading. Then, the performance of the two approaches is compared for the case of a seismic wave loading passing through a saturated soil column with different relative densities, revealing several differences between the results of the two models.

Keywords: Multi-scale, DEM, Toyoura sand, seismic waves propagation, Bounding surface plasticity, inertial effect

*Corresponding author
Email address: jerome.duriez@inrae.fr (J. Duriez)

1. Introduction

Proper numerical simulations of cyclic and seismic loadings, including liquefaction phenomena, are an important issue for the safety of any earth structure. Different strategies can be used to simulate a soil seismic response numerically. First, classical elastoplastic constitutive models such as Mohr-Coulomb and Cam Clay (Roscoe and Burland, 1968) models can reproduce the monotonic behavior of different soils under drained and undrained conditions with different levels of precision. However, the features of these models are not rich enough to directly simulate the cyclic phenomena during seismic loading (e.g., the irrecoverable volumetric strains produced by cyclic loading are not taken into account). The first strategy for cyclic modeling involves using such simple models in conjunction with damping (hypoelasticity) (Woodward and Griffiths, 1996) and an ad-hoc relation that relates the increment of the plastic volumetric strain per cycle to the number of cycles by an empirical formulation as shown by (Martin et al., 1975; Byrne, 1991). This method is easy to implement and can provide an overall quantitative description of the cyclic response of soils but it cannot give an accurate description. Second, kinematic hardening is recognized as a fundamental element for reproducing the cyclic behavior of soils. Comprehensive and elaborated constitutive models such as DM04 (Dafalias et al., 2004), CJS (Duriez and Vincens, 2015), P2PSand (Cheng and Detournay, 2021) and numerous other approaches in Kutter et al. (2019) used the kinematic hardening to reproduce an evolving soil behavior during cyclic loading, being caused by microstructural hardening mechanisms such as an evolution of fabric. This feature allows the models to follow the degradation of the material during cyclic loading.

Finally, the DEM approach is shown to be able to reproduce most of the soil features during monotonic and cyclic loading (Mohamed et al., 2022; Sibille et al., 2019; Gu et al., 2020; Xie et al., 2022) including the liquefaction phenomenon by using three or four contact parameters at the interparticle level depending on shape descriptions. In principle, the DEM deals with the real physics of granular media in which each particle is represented by its shape, mass, and inertia so that it can be a robust technique for studying the behavior of soils under cyclic and dynamic loadings and can also address all the shortcomings of phenomenological models that come from different hardening mechanisms.

Recently, many publications have proposed the multi-scale approach (Kouznetsova et al., 2002; Nguyen et al., 2014; Guo and Zhao, 2014; Nitka et al., 2009; Liu et al., 2016; Kuhn, 2022) to describe soil behavior in a boundary value problem (BVP) using information from the micro level via the discrete element method. In essence, finite element or finite volume codes provide a numerical solution for the differential equations for a continuous medium as seen at the BVP-scale. At some point in the numerical scheme, i.e., before solving the equation of motion, a constitutive relation is required to present the internal stresses. To this end, the constitutive response of the material is derived through direct DEM computations on the representative elementary volume (REV) attached to each Gauss point in the mesh without adding any empirical relationships.

In this study, we establish an information-passing coupling between a discrete element and a finite volume continuum code by which the constitutive response of the material is derived through direct DEM computations on a representative elementary volume (REV) attached to each mesh zone. The two codes used are: 1- FLAC3D (Itasca, 2019): a multi-dimensional Lagrangian explicit finite volume program to study numerically the mechanical behavior of a continuous three-dimensional medium (macro-scale). 2- PFC (Itasca, 2018): a program that models the movement and interaction of stressed assemblies of rigid particles with different shapes using the Distinct-Element Method (micro-scale).

For the multi-scale modeling, the stress homogenization formulation for the representative elementary volume REV is an essential element (Weber, 1966; De Saxcé et al., 2004; Bagi, 2003). For this purpose, we review the definition of the stress tensor for granular materials during dynamic events such as seismic and shock loadings for proper inclusion of the effect of shear strain rate and particle inertia on the mechanical behavior of granular media.

Then, we propose and discuss a multi-scale discrete-continuum modeling approach for the propagation of seismic waves through a saturated soil column made of Toyoura sand, a case study similar to the one by Taiebat et al. (2010) and multi-scale FDM-DEM method proposed by Kuhn (2022), in comparison with the direct use of an advanced elastoplastic model P2PSand (Cheng and Detournay, 2021; Itasca, 2019) in FLAC3D. It is worth noting our use of P2PSand model relates with other previous studies using advanced elastoplastic constitutive models in FLAC/FLAC3D to model wave propagation and liquefaction, such as the SANISand (Yang et al., 2020) and UBCSAND (Tsiaousi et al., 2020) models. Finally, we investigate the predictions of these two methods for the occurrence of the so-called "dynamic liquefaction" for a loose soil column after a fair quantitative calibration and validation process of the two numerical approaches at the sample scale under monotonic and cyclic loadings.

The article consists of four main sections. Section 2 describes the P2PSand constitutive model and its predictions for monotonic and cyclic loadings. Section 3 presents the DEM model previously developed by Mohamed et al. (2022) and herein used in the multi-scale framework as well as its calibration and validation for different monotonic and cyclic loading paths and points out the importance of a proper stress homogenization formula for dynamic loadings. Section 4 discusses the multi-scale modeling implementation and presents the validation of the latter when considering laboratory tests under different loading paths for drained and undrained conditions. Section 5 shows and discusses the comparison between the two approaches for the propagation of seismic waves as well as the effects of the DEM damping and particle sizes on the response of the multi-scale model.

2. P2PSand constitutive model

2.1. Model overview

The P2PSand model (practical two-surface plastic sand) has been developed for general 3D geotechnical earthquake engineering applications by (Cheng and

Detournay, 2021; Itasca, 2019). The model follows critical state plasticity within a bounding surface framework (Dafalias et al., 2004) through the inclusion of a scalar state parameter (Been and Jefferies, 1985) for sand. The state parameter of the present model is chosen as the pressure ratio index I_p which is defined in the $D_r - p'$ as the ratio between the current mean pressure p' and the corresponding critical state mean pressure plane for the same relative density value D_r. The relative density is indeed used instead of the void ratio inside all the equations of the model because it is directly reachable from in-situ tests.

In the deviatoric plane π (Fig. 1), the elastic domain is limited by a small circular yield surface that does not change in size during loading (no isotropic hardening is allowed) with a kinematic hardening tensor $\boldsymbol{\alpha}$ which is the center of this circle. The yield surface is actually described by the same function as in DM04 model (Dafalias and Manzari, 2004):

$$f = [(\boldsymbol{s} - p\boldsymbol{\alpha}) : (\boldsymbol{s} - p\boldsymbol{\alpha})]^{0.5} - \sqrt{2/3}pm = 0 \quad (1)$$

Where m is the size of the yield surface and is used as a fixed value of $m = 0.02M_{comp}$. M_{comp} is the critical-strength parameter for the triaxial compression path. p is the effective mean stress (isotropic stress) and $\boldsymbol{s}$ is the deviatoric stress tensor.

Besides the yield surface, the model incorporates four other surfaces in the normalized π plane as shown in Fig. 1. A constant critical state surface, bounding and dilatancy surfaces follow the same form as the bounding surface model proposed by Dafalias et al. (2004) with a Lode angle dependency. By shearing towards the critical state, the bounding and dilatancy surfaces evolve until they coincide with the critical state surface. In addition, an isotropic memory surface has the same shape as the bounding or dilatancy surface. Its size is determined by the historic position of $\boldsymbol{\alpha}$. The main purpose of this last surface is to avoid overshooting behavior during reversal loadings. Finally, the detailed formulations of the P2PSand model are given in Appendix A.

Table 1 presents the dimensionless parameters of the P2PSand model. The model adopts a unique critical state line that is defined based on the finding

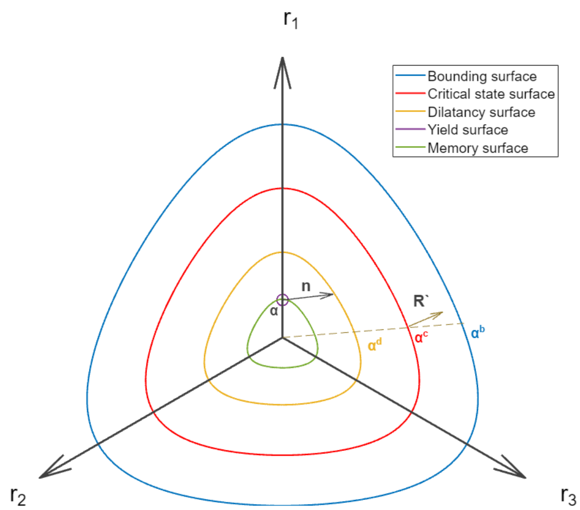

Figure 1: Schematic of different surfaces in the π plane for the P2PSand model after (Cheng and Detournay, 2021).

of Li and Wang (1998) with three parameters D_{rc0}, λ_c and ζ. While for the critical strength, the parameter c represents the ratio between extension and compression triaxial critical strengths. n_b and n_d are two model parameters that are used to determine the size of the bounding and dilatancy surfaces. The rate of plastic strains is controlled by two parameters, h_0 is the plastic shear rate and A_{d0} is the plastic volumetric rate. Also, the plastic volumetric rate is impacted by the evolution of fabric with an evolving rate depending on the C_z parameter until reaching maximum fabric magnitude z_{max}. The previous two parameters could be internally defined by the model or to be inserted directly by the user. Finally, K_{cyc} parameter intervenes when the state of the kinematic hardening tensor $\boldsymbol{\alpha}$ is inside the memory surface in Fig. 2 to capture the sand behavior by which dilation/contraction evolution rate is lower during cyclic loading compared to virginal loading.

2.2. Calibration and validation of the P2PSand model for different monotonic and cyclic loadings

The essence of elastoplastic models is that strains are divided into elastic and plastic components and it can be considered that plastic deformations are

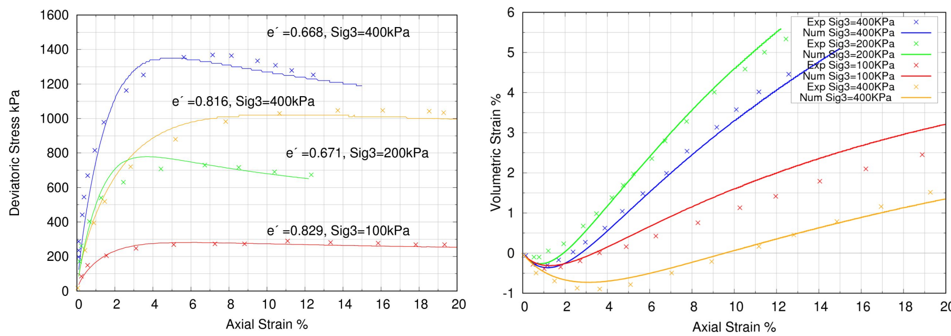

Figure 2: Results of P2PSand model for Toyoura sand along drained triaxial compression for various initial void ratios and initial mean pressure with one calibration test ($\sigma_3 = 400$ kPa and initial void ratio $= 0.668$) and three other validation tests. Experimental data from Fukushima and Tatsuoka (1984).

responsible for the evolution of pore pressure in undrained conditions and, as a result, for the loss of material strength in such conditions often encountered in practice. Therefore, the calibration of the elastoplastic models should be based on stress paths that make it possible to distinguish between the elastic and plastic strains e.g drained tests with several loading and unloading intermediate paths or undrained tests. Here, the calibration of the P2PSand model parameters for Toyoura sand (Table 1) is performed based on one drained and one undrained triaxial compression test. For this calibration phase, Fig. 2 represents the results of the P2PSand model together with experimental data from Fukushima and Tatsuoka (1984) for triaxial drained compression tests for various initial void ratios and confining pressures. The model presents a close fit with the corresponding experimental results for the deviatoric stress and volumetric strain responses by introducing the effect of different initial void ratio values on mechanical behavior. During undrained tests, the model results are assessed for compression triaxial tests in Fig. 3 together with experimental data from Yoshimine et al. (1999). The results of the undrained compression tests can validate with good precision the experimental data.

Afterwards, the predictive abilities of the model under cyclic triaxial tests are evaluated. Actually, one parameter in Table 1 k_{cyc} should still be calibrated at this stage. Therefore, the model is calibrated for one cyclic test and validated

Table 1: P2PSand model dimensionless parameters for Toyoura sand with $D_r \in$[0,1]

Criteria	Parameter Symbol	Toyoura sand
Elastic-moduli	G_0	200
	C_{Dr}	0.8
	n	0.5
	ν	0.12
Critical state line	D_{rc0}	0.145
	λ_c	0.035
	ζ	0.7
Critical state surface	ϕ_{comp}	32°
	c	0.7
Bounding surface	n^b	0.13
Dilatancy surface	n^d	0.2
Hardening model	h_0	1.1
Dilatancy	A_{d0}	0.65
Fabric influence	C_z	$G_0(D_r + C_{Dr})$
	Z_{max}	$21D_r^{3.85}$<15
Cyclic Loading	k_{Cyc}	0.4

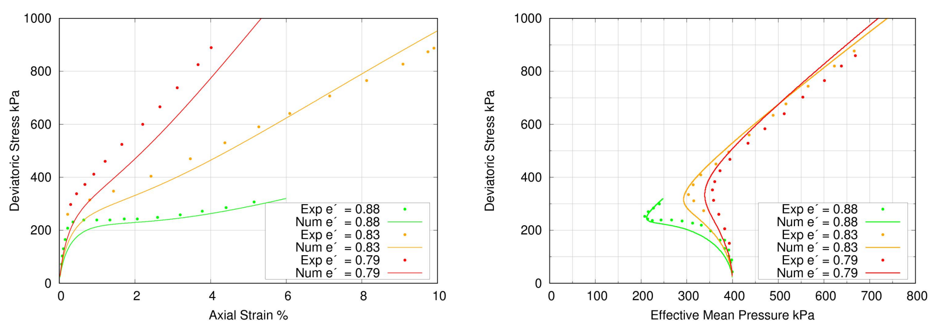

Figure 3: Results of P2PSand model for Toyoura sand along undrained triaxial compression for various void ratios with one calibration test σ_3 = 400 kPa and void ratio = 0.79 and two other validation tests. Experimental data from Yoshimine (2013).

for another cyclic test. Wang et al. (2016) provided the experimental data for Toyoura sand prepared using the air-pluviation method, which is consistent with the previous samples used by (Fukushima and Tatsuoka, 1984) for monotonic loadings. The experimental data are for different cyclic triaxial tests with different densities and cyclic stress ratios CSR=$q/2p_0$ (ratio between cyclic deviatoric stress amplitude and initial confining pressure) as shown in Fig. 4 and Fig. 5 respectively. The results demonstrate that there are still some difficulties in following the exact same evolution as the experimental data at the different stages of the test. Also, the P2PSand model shows a bias in the deviatoric stress vs axial strain curve by which the axial strain accumulates progressively on the extension side of the curve. Nevertheless, the model gives acceptable predictions in terms of the number of cycles required to reach liquefaction (i.e., zero mean effective stress) and liquefaction phenomena simulation (the progressive decrease in effective mean pressure and the butterfly shape) compared to the experimental data. Indeed, for these two tests with CSR=0.147 and 0.163 the numbers of cycles required to attain an axial strain value of about ϵ_a= 9% are ($N_{Exp} = 37, N_{P2PSand} = 32$) and ($N_{Exp} = 12, N_{P2PSand} = 17$) respectively.

3. 3D-DEM model for Toyoura sand

3.1. Model formulation and generation procedure

A DEM model for Toyoura sand previously presented in (Mohamed et al., 2022) is used. It includes a constant-stiffness rolling resistance contact model with 4 parameters and spherical particles that follow the same particle size distribution as Toyoura sand as shown in Fig. 6 (model 1) except for a scaling factor that was mechanically inconsequential by virtue of the contact model in the quasi-static cases. However, in the present context where dynamic effects are anticipated to take place, we also consider the exact granular size distribution as shown in Fig. 6 (model 2, differing from model 1 only in that aspect).

DEM samples are created by starting with a cloud of non-overlapped particles within rectangular parallelepiped rigid walls. The walls are then moved inwards in order to reach a target compaction pressure. A 3D-DEM REV with

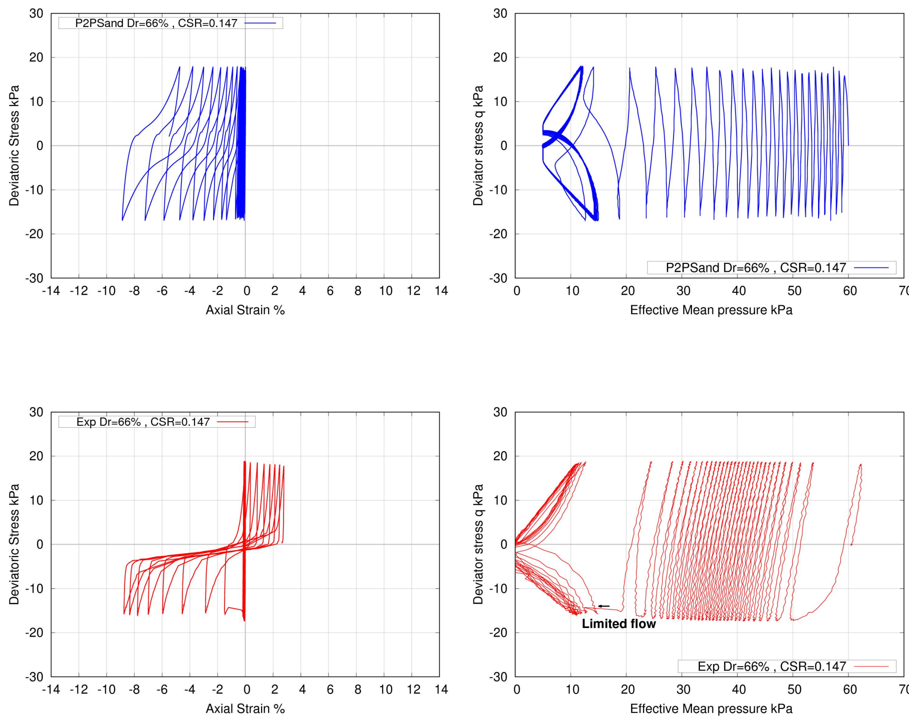

Figure 4: (Top) Results of the P2PSand model for an undrained cyclic triaxial test for Toyoura sand sample with $D_r = 66\%$ and CSR=0.147 serving as calibration. (Bottom) Experimental data from Wang et al. (2016).

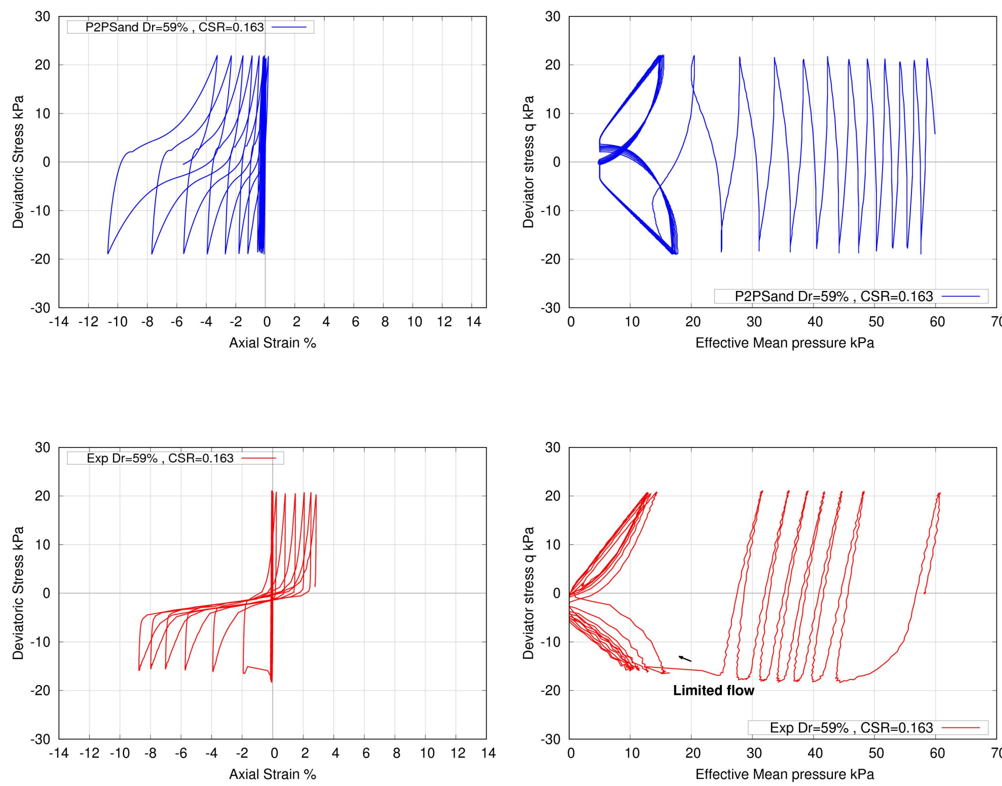

Figure 5: (Top) Results of the P2PSand model in a validation stage for an undrained cyclic triaxial test for the Toyoura sand sample with $D_r = 59\%$ and CSR=0.163. (Bottom) Experimental data from Wang et al. (2016).

a number of N_b=7000 particles is used for the current multi-scale modeling of Toyoura sand, as it was proven by Mohamed et al. (2022) that this number is sufficient to give a homogeneous distribution of the void ratio inside the sample and an unaffected stress-strain response when the number of particles exceeds this value. It is worth mentioning that considered DEM samples always show the same initial void ratio values as the reference lab experiments. Reaching such given initial void ratio values is achieved during that compaction phase based on the friction coefficient and rolling coefficient values, which are tuned independently of the subsequent shear loading phase. The contact parameters and packing properties, including a zero initial anisotropy due to the isotropic generation, are summarized in Table 2. The corresponding DEM and P2PSand relative density values are calculated based on the maximum and minimum void ratio values $e_{min} = 0.6$ and $e_{max} = 1$ of Toyoura sand.

Following Mohamed et al. (2022) who provided a detailed presentation, the rolling resistance contact model with 4 contact parameters is used as shown in Table 2, where E_{mod}, K_n, K_s are effective modulus i.e. the constant normal stiffness scaled with respect to (divided by) particle size, the actual normal stiffness and its tangential counterpart. The friction μ and rolling friction μ_r coefficients are imposed on the contact to limit shear force and moment.

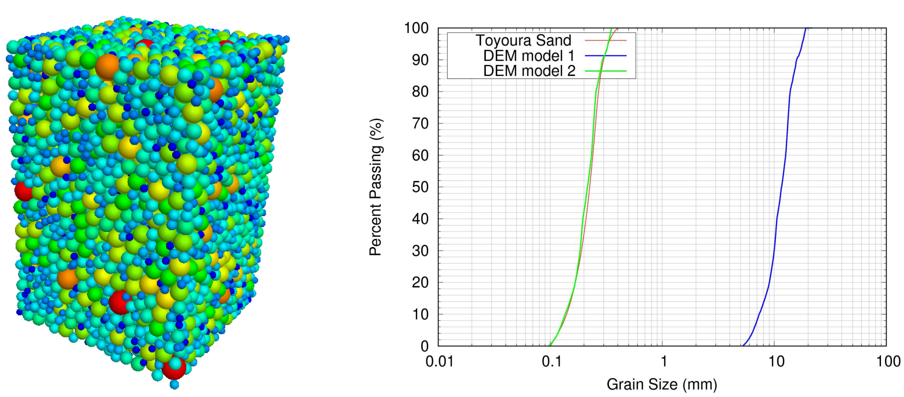

Figure 6: Left: Toyoura sand 3D-DEM model where different colors refer to different diameters. Right: different particle size distributions for DEM (model 1 and model 2) vs Toyoura sand from Dong et al. (2016)

Table 2: 3D-DEM model parameters for different DEM and multi-scale simulations

Contact				Packing (see also Fig. 6 for psd)			
E_{mod} (MPa)	K_n/K_s (-)	μ (-)	μ_r (-)	N_b (-)	Initial anisotropy	Grain mass density (kg/m^3)	Relative density (%)
400	3	0.6	0.38	7000	Variable (0 for lab tests)	2600	Variable

3.2. Calibration and validation of the 3D-DEM model for monotonic loadings

The calibration of the used DEM model for Toyoura sand was performed in (Mohamed et al., 2022) based on a drained triaxial test. During the validation process, the model was therein validated to fit other experimental data of drained and undrained triaxial tests (compression and extension). The results of the drained triaxial tests were in good accord with the corresponding experimental data for the different triaxial compression tests with different initial void ratio values. One may note that during the undrained extension triaxial tests, the model showed less ability to lose effective strength when compared to the experimental data, unlike another polyhedra-based model also proposed in (Mohamed et al., 2022). However, we stick here to the sphere-based model due to the computational costs of multi-scale simulations.

3.3. Validation of the DEM model under cyclic loading

In line with the present focus on seismic loadings, the predictions of the DEM model for different undrained cyclic tests are herein investigated. The predictions of the DEM approach and two experimental data for two undrained cyclic triaxial tests Wang et al. (2016) with different values of CSR = 0.147 and 0.163 and initial $p' = 60$ kPa are shown in Fig. 7 and 8. For these two tests with CSR=0.147 and 0.163 the number of cycles required to attain an axial strain value of about ϵ_a= 9% is ($N_{Exp} = 37, N_{DEM} = 40$) and ($N_{Exp} = 12, N_{DEM} = 20$) respectively. Compared to monotonic loadings, less accurate predictions are observed compared with the experimental data since the initial plastic flow is initiated on the compression side, which may be attributed to different initial fabric anisotropies when compared to the experimental data. Nevertheless, the DEM model gives satisfactory results since it doesn't exhibit the illogical behavior that was observed previously by using the P2PSand model, particularly the evolution in one direction in the deviatoric vs axial strain $q-\epsilon_a$ plane, the discontinuity in $q-\epsilon_a$ and deviatoric stress vs effective mean pressure $q-p'$ planes and the non-occurrence of limited flow before liquefaction.

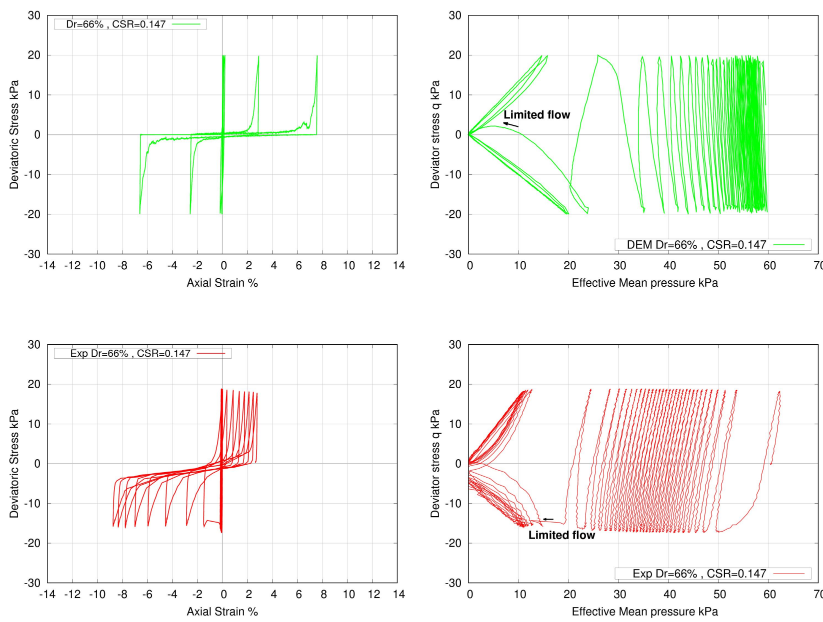

Figure 7: Deviatoric stress versus axial strain and effective pressure in undrained cyclic triaxial tests of Toyoura sand, with initial p'=60 kPa and Dr =0.66, CSR=0.147 — comparison of DEM results (solid green) with experimental data from Wang et al. (2016) (solid red).

3.4. Review of homogenization formulas for the stress tensor of a DEM packing including dynamic effects

To make a step from micro- to macro-scale, the REV stress response is computed using the stress homogenization formula (Weber, 1966; Christoffersen et al., 1981) for the static part contribution of a stressed particle assembly as follows:

$$\boldsymbol{\sigma}^W = -\frac{1}{V}\sum_{N_c}\mathbf{F}^{(\mathbf{c})}\otimes\mathbf{L}^{(\mathbf{c})} \tag{2}$$

where V and N_c are the packing volume and the number of contacts inside that volume respectively. $\mathbf{F}^{(\mathbf{c})}$ and $\mathbf{L}^{(\mathbf{c})}$ represent the contact force and branch vector

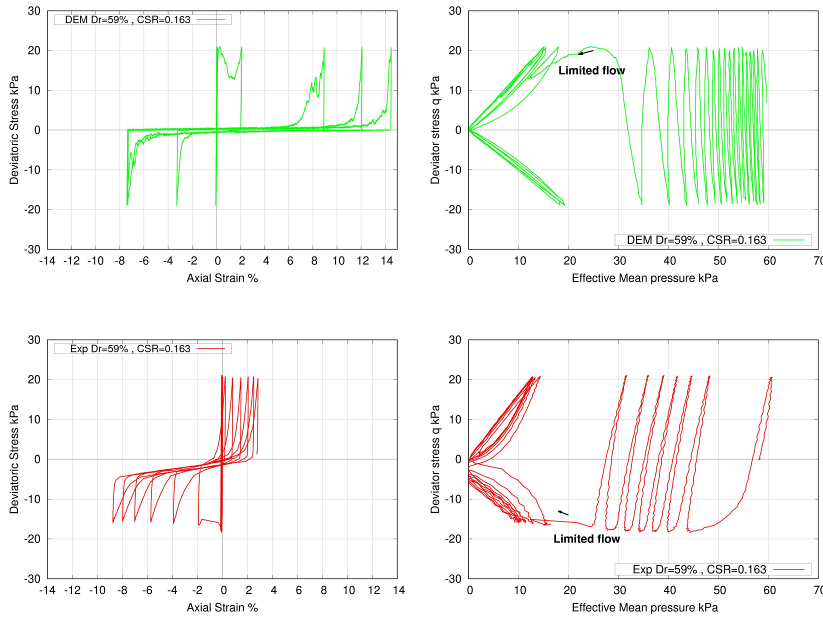

Figure 8: Deviatoric stress versus axial strain and effective mean pressure in undrained cyclic triaxial tests of Toyoura sand, with initial p'=60 kPa and Dr =59%, CSR=0.163 — comparison of DEM results (solid green) with experimental data from Wang et al. (2016) (solid red).

respectively.

As highlighted by (Yan and Regueiro, 2019; Duriez and Wan, 2017), the effect of boundary contacts cannot be neglected for a relatively small number of particles in REV. Bagi (2003) proposed a stress tensor formula that takes into account the external contact forces as follows:

$$\boldsymbol{\sigma}^B = -\frac{1}{V}\left(\sum_{N_c}\mathbf{F}^{(\mathbf{c})}\otimes\mathbf{L}^{(\mathbf{c})} + \sum_{N\in E}\mathbf{F}^{(\mathbf{N})}\otimes\mathbf{L}^{(\mathbf{N})}\right) \tag{3}$$

where E denotes particle contacts that lie on the boundary of the REV and $\mathbf{L}^{(\mathbf{N})}$ is the branch vector of the external contact point.

The applications of the current multi-scale modeling are oriented to seismic analysis where dynamic effects i.e., inertial terms, should not be neglected. De Saxcé et al. (2004) take into account those inertial terms, together with the effect of body forces, as follows:

$$\boldsymbol{\sigma}^D = -\frac{1}{V}\left(\sum_{N_c}\mathbf{F}^{(\mathbf{c})}\otimes\mathbf{x}^{(\mathbf{c})} + \sum_{N\in E}\mathbf{F}^{(\mathbf{N})}\otimes\mathbf{L}^{(\mathbf{N})} + \int_V \rho\boldsymbol{x}\otimes(\boldsymbol{g}-\boldsymbol{a})dV\right) \tag{4}$$

where $\boldsymbol{x}$ denotes the spatial coordinates while ρ, $\boldsymbol{g}$ and $\boldsymbol{a}$ are mass density, gravitational and inertial accelerations respectively. For the present multi-scale simulations where materials may be subjected to severe dynamic actions i.e., earthquakes and impact loadings, the stress tensor formula in Eq. 4 is adopted, as justified below.

3.5. Numerical investigation of inertial effect

The purpose of this section is to check the previous homogenization equation by considering one example where dynamic effects occur. Five triaxial drained tests are performed with different strain rate values and shown in Fig. 9, corresponding to different values of inertial number I as defined by Da Cruz et al. (2005):

$$I = \frac{\dot{\epsilon}_a D}{\sqrt{\frac{p'}{\rho}}} \tag{5}$$

where $\dot{\epsilon}_a$ is the axial strain rate, D the average particle diameter, p' is the effective pressure and ρ is the density. The DEM model 2 in Fig. 6 is utilized and the details of the numerical parameters are shown in Table 2. First, in Fig. 9 the contribution of each term of the stress tensor is investigated in order to examine how dynamic effects may influence and modify the average stress tensor. The deviatoric stress is calculated in two different ways, first, from the average stress values of the pair of boundary walls along each direction, and second, from the stress homogenization formula in Eq. 4. The results highlight the importance of the inertial part in Eq. 4 and show a significant difference between the static and dynamic definitions of stress tensors for the case of the most dynamic loading. In a second analysis in Fig. 10 showing the macroscopic sample behavior for all cases, one can see that, by increasing the inertial number of the simulation, the apparent modulus and deviatoric stress increase significantly, resulting in a more dilative response. In addition, no stable critical state can be achieved for the most dynamic case ($I \in [4 \times 10^{-2}; 10^{-1}]$). Finally, while the three tests with the lowest strain rate values ($I < 2 \times 10^{-2}$) have very similar overall responses in the $q - \epsilon_a$ and $\epsilon_v - \epsilon_a$ curves, it should be noted that, as shown in Fig. 10, changing the inertial number in that interval still has a significant impact on the apparent modulus at the initial stage of these tests and that being closer to a quasi-static regime requires $I \approx 10^{-3}$.

These values are coherent with those of Da Cruz et al. (2005) who demonstrated that a quasi-static critical state regime with almost no variation in the effective friction coefficient requires very low values of I=10^{-3} and that a fully collisional flow regime occurs for I=10^{-1}.

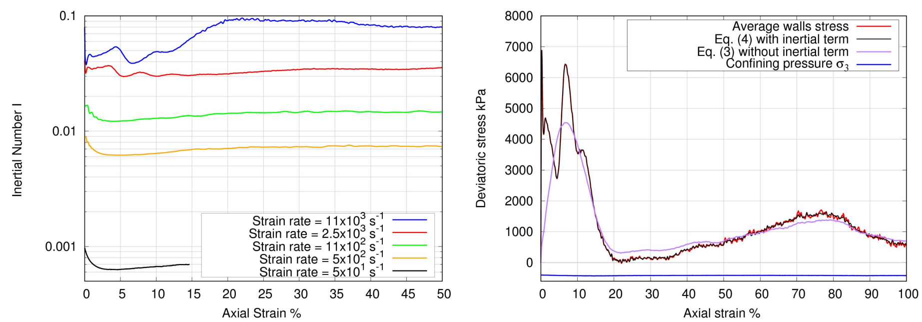

Figure 9: Left: inertial number during five different drained triaxial tests (σ_3 = 400 kPa and initial n = 0.388) with different values of strain rate. Right: Inertial term effect on deviatoric stress vs axial strain curve for strain rate = 11×10^3 s^{-1}.

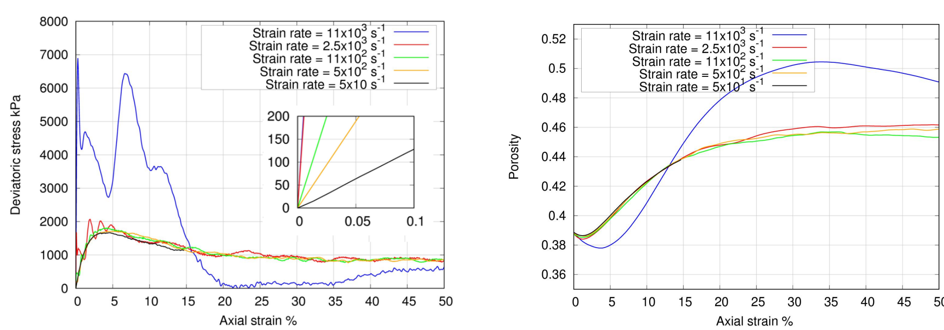

Figure 10: The effect of various strain rates and inertial number values on the macroscopic behavior of a drained triaxial test with σ_3 = 400 kPa and initial n = 0.388 enclosing a magnified scale for the initial part of the deviatoric curve for the different tests.

4. Multi-scale coupling method

4.1. Flac3D continuum model

The continuum medium in Flac3D is discretized into constant strain-rate elements with a tetrahedral shape. The general numerical scheme is shown in Fig. 11. At the beginning of each time step, the strain rate tensor $\dot{\boldsymbol{\epsilon}}$ is defined from nodal velocities. Then a constitutive relation is applied to define the new stress tensor $\boldsymbol{\sigma}$. Finally, the equation of motion is applied to compute the new nodal velocities and therefore the new nodal displacement. The finite volume formulation of Flac3D is presented in detail in Appendix B.

4.2. Multi-scale coupling of Flac3D and PFC

In this section, a two-scale numerical homogenization approach by FVM×DEM (in Flac3D and PFC software) is presented. Simultaneous running and computation are performed by these two codes. A unique DEM packing is assigned as a REV bounded with rigid walls for each zone of Flac3D and the strain rate tensor of each Flac3D zone is applied to each corresponding REV. Mainly, a new plug-in c++ constitutive model is constructed in Flac3D to invoke a PFC computation and to offer the new stress state to the Flac3D continuum model at each timestep. In the present context between Flac3D and PFC, the strain rate tensor $\dot{\boldsymbol{\epsilon}}$ is conserved and not only the strain increment $\boldsymbol{d\epsilon}$ to take into account the inertial and viscous effects (if a viscous contact model would be applied) in the behavior of granular mass (Jop et al., 2006).

Fig 11 shows the computational homogenization scheme applied to each time step. It is worth noting that unlike coupling of DEM with the finite element method (FEM×DEM, Nguyen et al., 2017), the present scheme does not need to establish a consistent tangent stiffness matrix from a DEM computation and it is enough to update the stress matrix in the continuum model at each time step based on the DEM computations.

Finally, the 3D-DEM REV presented previously in Section 3 with a number of 7000 particles is used for the current multi-scale modeling of Toyoura sand, as

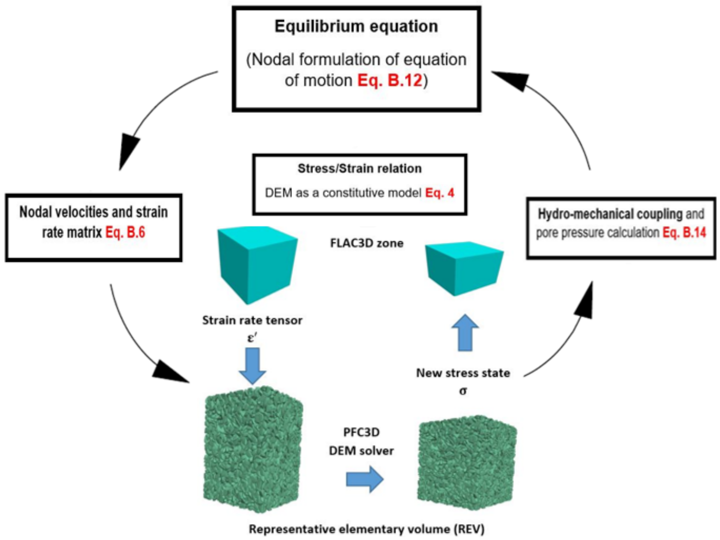

Figure 11: General Flac3D cycle in black and computational homogenization scheme Flac3D-PFC inset in color.

it was proven by Mohamed et al. (2022) that it is sufficient to give an unaffected stress-strain response when the number of particles exceeds this value.

4.3. Validation of the multi-scale implementation under drained-undrained triaxial and simple shear tests for Toyoura sand

A verification procedure is first introduced on very simple cases with 1 or 2 adjacent zones to check the correct implementation of the DEM–FVM coupling scheme. The predictions of corresponding Flac3D models for drained and undrained triaxial tests for loose and dense samples are tested. Fig. 12(a) shows the macroscopic response of a dense Toyoura sand sample ($D_r = 90\%$) until reaching the critical state condition. The results demonstrate stable numerical results at the different stages of the test (including the strain softening regime) until the critical state. In addition, the macroscopic response of each zone is shown to be identical to the corresponding REV response. As for the loose sample, a similar simulation is performed to check the numerical stability of the scheme for a case where more grain rearrangement and plastic deformation are anticipated to take place. Fig. 12(b) shows the results of a triaxial test for a relatively loose Toyoura sand sample $D_r = 40\%$. The results again confirm the stability of the coupling scheme for the deviatoric and volumetric strain curves.

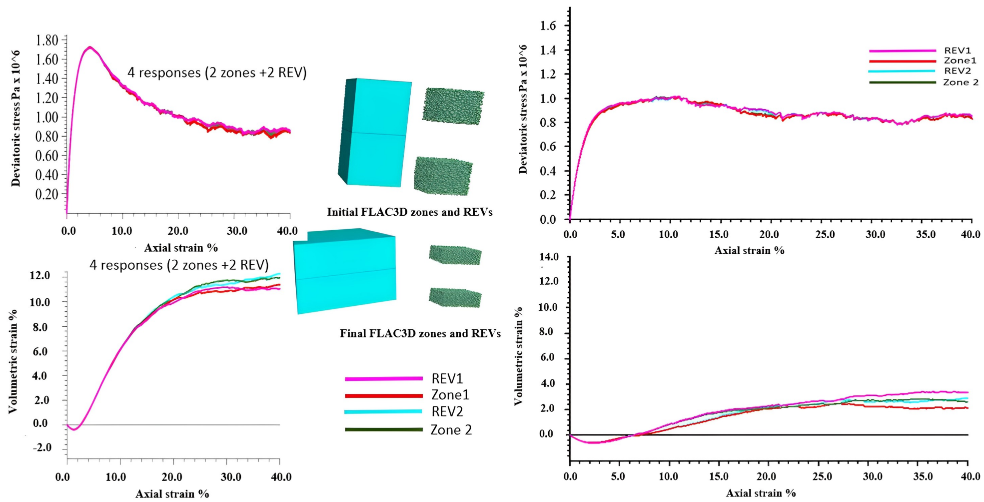

(a) Dense $D_r = 90\%$

(b) Relatively loose $D_r = 40\%$

Figure 12: Deviatoric stress vs axial strain and volumetric strain vs axial strain for Toyoura sand with initial confining pressure = 400 kPa and two different initial porosity values.

Furthermore, a hydro-mechanical analysis is considered for an undrained triaxial test condition and is imposed in the Flac3D model where the pore pressure is generated due to the mechanical volumetric deformation and given water compressibility $k_f = 2$ GPa and $\alpha_{Biot} = 1$ (see Itasca (2019) and Appendix B) in a classical simplified version of the pore pressure update method proposed by Kuhn and Daouadji (2020). The results of the multi-scale model are shown in Fig 13 for an undrained condition for a loose sample with an initial confining pressure = 400 kPa. Results show almost similar responses for the undrained test using only the DEM and constant volume boundary condition presented in Mohamed et al. (2022). Also, a unique behavior is observed for the REVs and Flac zones until a large axial strain value $\epsilon_a = 22\%$.

Finally, it is checked that the present use of rigid boundaries does not pre-

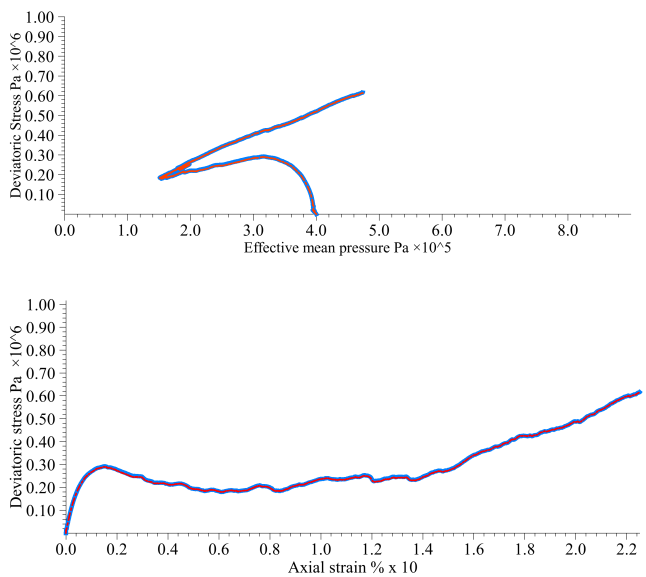

Figure 13: Deviatoric stress vs axial strain and effective mean pressure for a loose Toyoura sand sample (D_r = 25%) during an undrained triaxial test with an initial confining stress=400kPa. The responses of DEM (red) and Flac upper zone (blue) are identical.

clude correctly addressing non-axisymmetric simulations such as simple shear. Duriez et al. (2011) actually suggested with a similar DEM setup that possible localization bias was absent until a significant shear strain value γ=0.5, in spite of the rigid boundaries. Here, the coupling scheme is assessed for a simple shear test with a single zone in Fig. 14, under an initial isotropic stress of 400 kPa, a constant σ_{zz} = 400 kPa and an initial porosity value of n=0.41. The REV and Flac zone give identical results until a large value of shear strain $\gamma = 0.65$.

5. Multi-scale modeling of seismic wave propagation through a saturated soil column

5.1. Comparison of results from the multi-scale approach with the P2PSand-based classical approach

As the main application, a vertical column of saturated sand made up of ten 3D zones is considered to be shaken by an earthquake as shown in Fig. 15. The sandy material is described either with the DEM or the P2PSand models described in the previous sections. Before the application of the earthquake

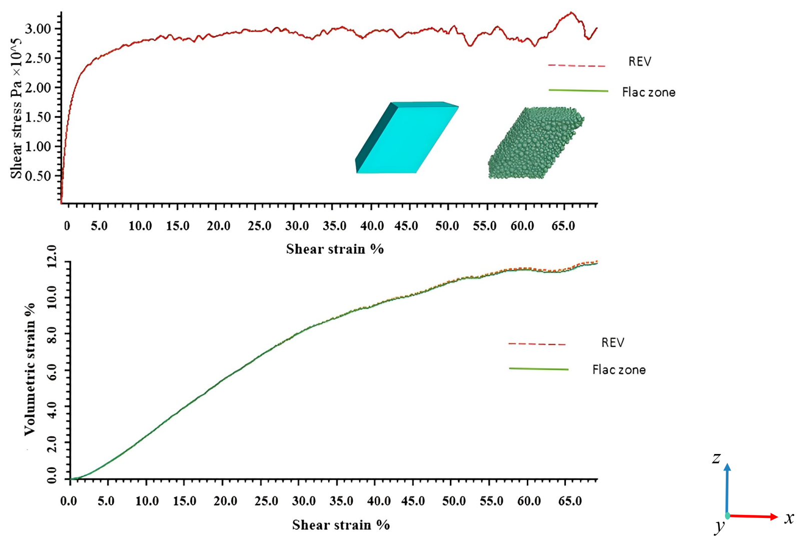

Figure 14: Simple shear test (constant σ_{zz}) with an initial isotropic stress of 400 kPa and an initial porosity value n=0.41.

wave, stresses are initialized to $\sigma_x = \sigma_y = 0.5\sigma_z$ inducing an initial anisotropic stress state all along the column. As with the previous undrained test, the pore pressure evolves throughout the fully saturated column in Flac3D only due to the mechanical volumetric change resulting from the seismic shaking. It is indeed assumed for simplicity that the characteristic time of the earthquake event is faster than the time required for the fluid to flow from one zone to another and Darcy's law and its diffusive effects are accordingly deactivated herein, even though a full hydro-mechanical coupling is technically possible in FLAC3D. The bedrock boundary condition is used at the bottom of the model and a constant lateral total stress is applied as a lateral boundary condition. In the case of using the P2PSand model, a 2% Rayleigh damping was employed while for the multi-scale model, a classical Cundall, i.e. global, damping (Cundall, 1987) with a 0.6 coefficient is used by default in the DEM, before being investigated in more detail in a forthcoming section. The earthquake loading is chosen as the Gilroy No.1 record of the 1989 Loma Prieta earthquake (which occurred on California's central coast), scaled to have a peak ground acceleration of 0.8 g in Fig. 15.

In order to analyze the models' response in light of the previous predictions of the models for cyclic triaxial tests (compression/extension) in Sections 2.2 and 3.3, it is chosen to apply the input acceleration at the bottom as a P-wave. The simulations are performed for two cases with different initial density values representing the relatively dense and loose states of Toyoura sand. The results of the comparison between the two models during the shaking phase for both cases are analyzed in terms of stress-strain responses and acceleration time history at different levels of the column.

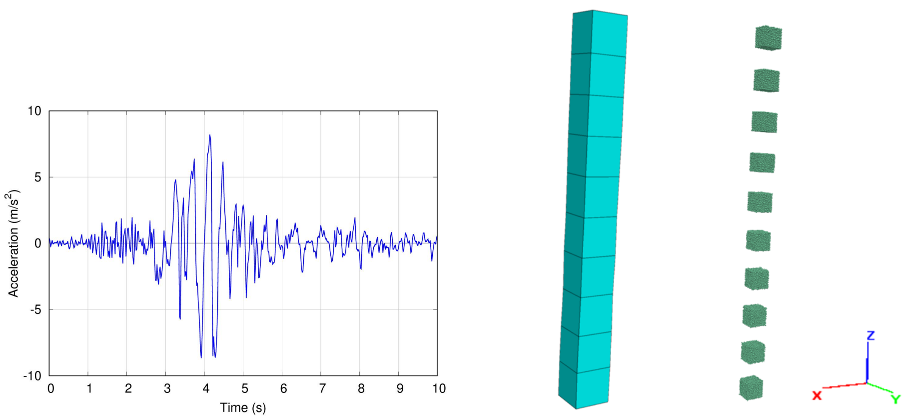

Figure 15: Left: The input vertical acceleration at the bottom zone. Right: the geometry of the Flac3D soil column and the corresponding REVs for multi-scale modeling.

Fig. 16 and Fig. 17 show the response of the soil column to the relatively dense soil $D_r = 60\%$ in terms of deviatoric stress vs axial strain and deviatoric stress vs effective mean pressure for the two models. As for the multi-scale, at the early stage of the shaking, an increase in the effective mean pressure is observed at the different levels due to the dilative tendency of the soil. However, later and during the intense waves, a slight decrease in the effective mean pressure is observed, coinciding with an accumulation of shear strains in all levels of the soil column, especially in the top zone. On the other hand, the response of the P2PSand model shows less ability to lose effective mean pressure and more tendency to accumulate axial strain only in the positive side (axial shortening) of the deviatoric stress vs axial strain curve.

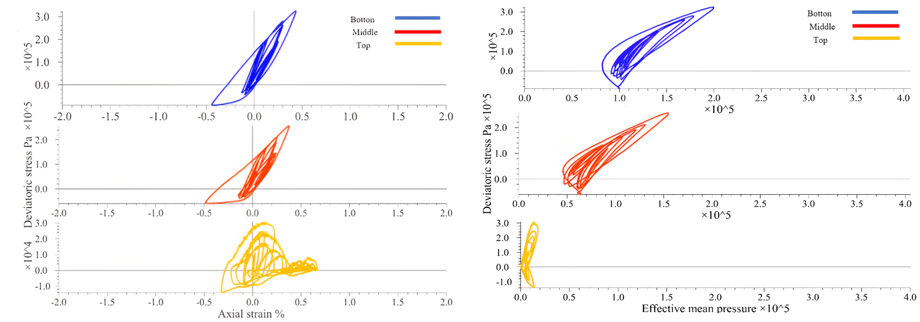

Figure 16: Multi-scale model predictions for a relatively dense soil column ($D_r = 60\%$). Left: deviatoric response at different positions of the soil column. Right: deviatoric stress vs effective mean pressure.

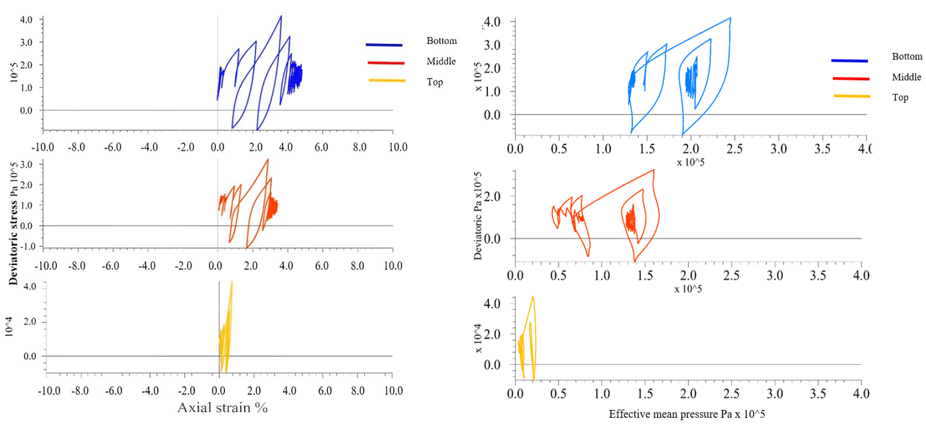

Figure 17: P2PSand model predictions for a relatively dense soil column ($D_r = 60\%$). Left: deviatoric response at different positions of the soil column. Right: deviatoric stress vs effective mean pressure.

The acceleration history is monitored at different levels and shown in Fig. 18. Results show that the base acceleration is transmitted to the surface of the soil column in two models, resulting in a large amplitude at the surface of the soil. The two models exhibit almost the same maximum acceleration at the bottom and middle zones, but a larger acceleration at the top zone is observed for the P2PSand model compared to the multi-scale model.

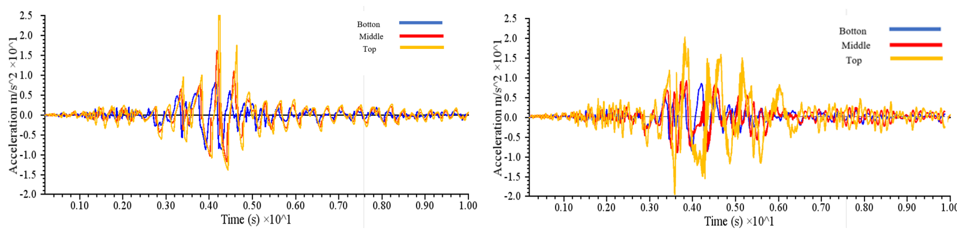

(a) P2PSand

(b) Multi-scale

Figure 18: Acceleration time history for the P2PSand and Multi-scale models at different positions for a dense soil column of Toyoura sand.

The second case investigated is for a loose soil column with a relative density of $D_r = 25\%$. The results of the two models are shown in Fig. 19 and Fig. 20. Despite the larger shear strain values observed for the P2PSand model in the bottom and middle zones as shown in Fig. 21, the results show that the liquefaction mechanism is also observed for the multi-scale model since the middle and top zones reach a zero effective mean pressure value during the event. In addition, the top zone of the multi-scale model shows higher axial and shear strains with $\epsilon_a \approx 4\%, \gamma \approx 6\%$ compared to the P2PSand model $\epsilon_a \approx 1.15\%, \gamma \approx 1.72\%$. Thinking of another, strain-based, liquefaction criterion such as proposed by Cappellaro et al. (2021) in terms of double-amplitude shear strain value $\gamma = 7.5\%$, one can note that this value that is not attained by the two models.

The acceleration responses for the loose case are shown in Fig. 22. The results of the two models are similar for the bottom and middle zones. However, more spike values are observed in the case of the multi-scale model at the top

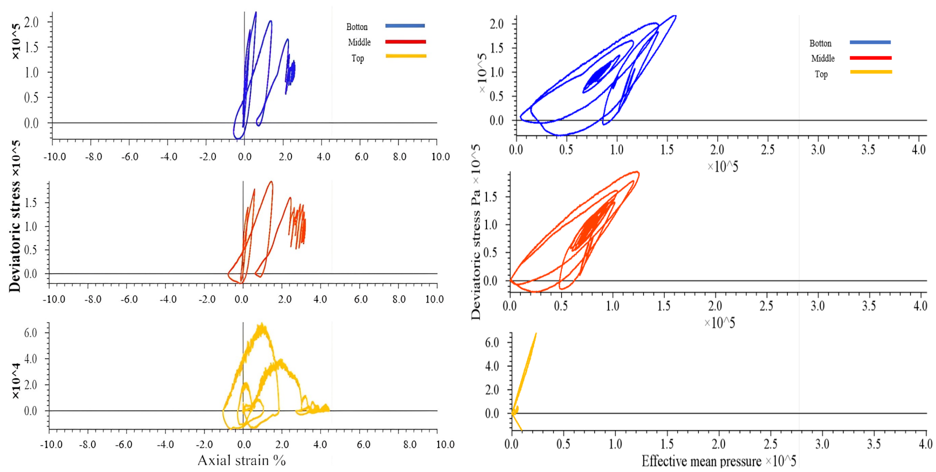

Figure 19: Multi-scale model predictions for a loose soil column ($D_r = 25\%$). Right: deviatoric stress vs effective mean pressure. Left: deviatoric response at different positions of the soil column.

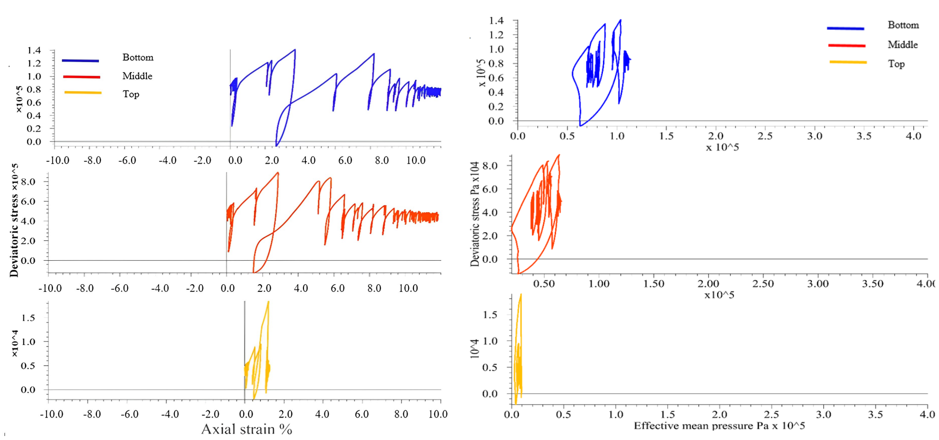

Figure 20: P2PSand model predictions for a loose soil column ($D_r = 25\%$). Left: deviatoric response at different positions of the soil column. Right: deviatoric stress vs effective mean pressure.

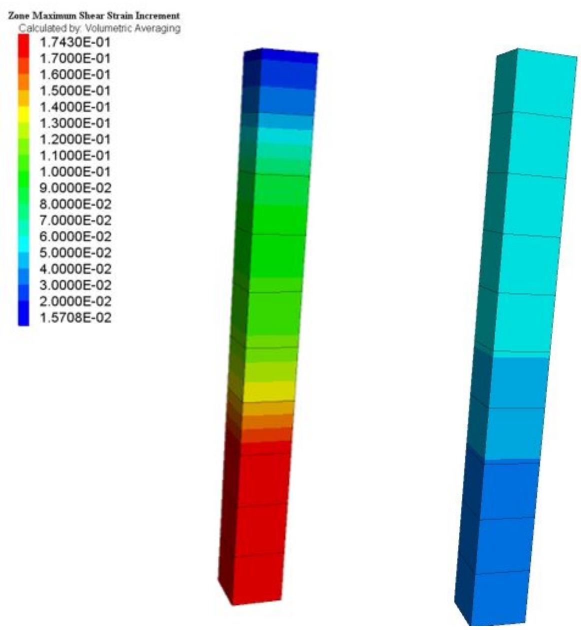

(a) P2PSand (b) Multi-scale

Figure 21: Shear strain profile along the soil column at T=10 s for the P2PSand and Multi-scale models for a loose soil column ($D_r = 25\%$).

zone due to the large deformation of this zone.

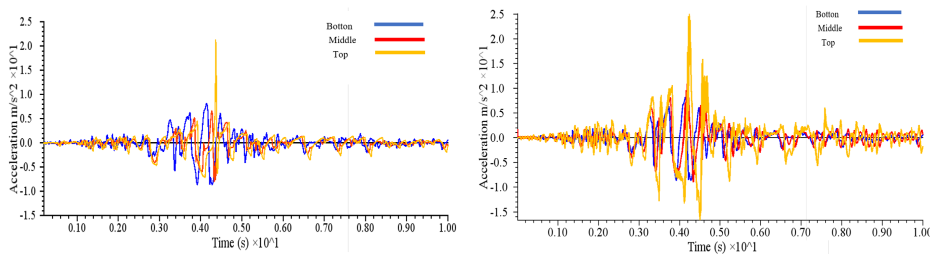

(a) P2PSand (b) Multi-scale

Figure 22: Acceleration time history for the P2PSand and Multi-scale models at different positions for a loose soil column of Toyoura sand.

In general, a clear contradiction is observed between the predictions of the two approaches since the large deformation occurs in the case of the multi-scale approach for the top zone, while the P2PSand model predicts a large deformation for the bottom zone. In addition, for the two studied relative density values, the multi-scale model gives lower axial strain at different positions, except for the top zone in the case of the loose case. Additionally, for the loose case, the multi-scale model shows acceleration amplification (Fig. 22) at the top zone when compared with the P2PSand model.

In addition to the macroscopic results, useful microstructure information can be elicited from the multi-scale model. Fig. 23 shows the evolution of the force networks for the loose soil column before and after the seismic event. Before the event, the vertical components of the force networks have the highest contact force, which is consistent with the initial anisotropic state of the samples. After the event, the top sample has a very weak force network due to liquefaction occurrence in this zone.

5.2. Parametric study on the damping coefficient and particle size

As for the multi-scale model, physically dissipative microscale phenomena such as contact friction serve as the main source of energy dissipation. As it is customary in DEM, a numerical Cundall damping is also herein present and may

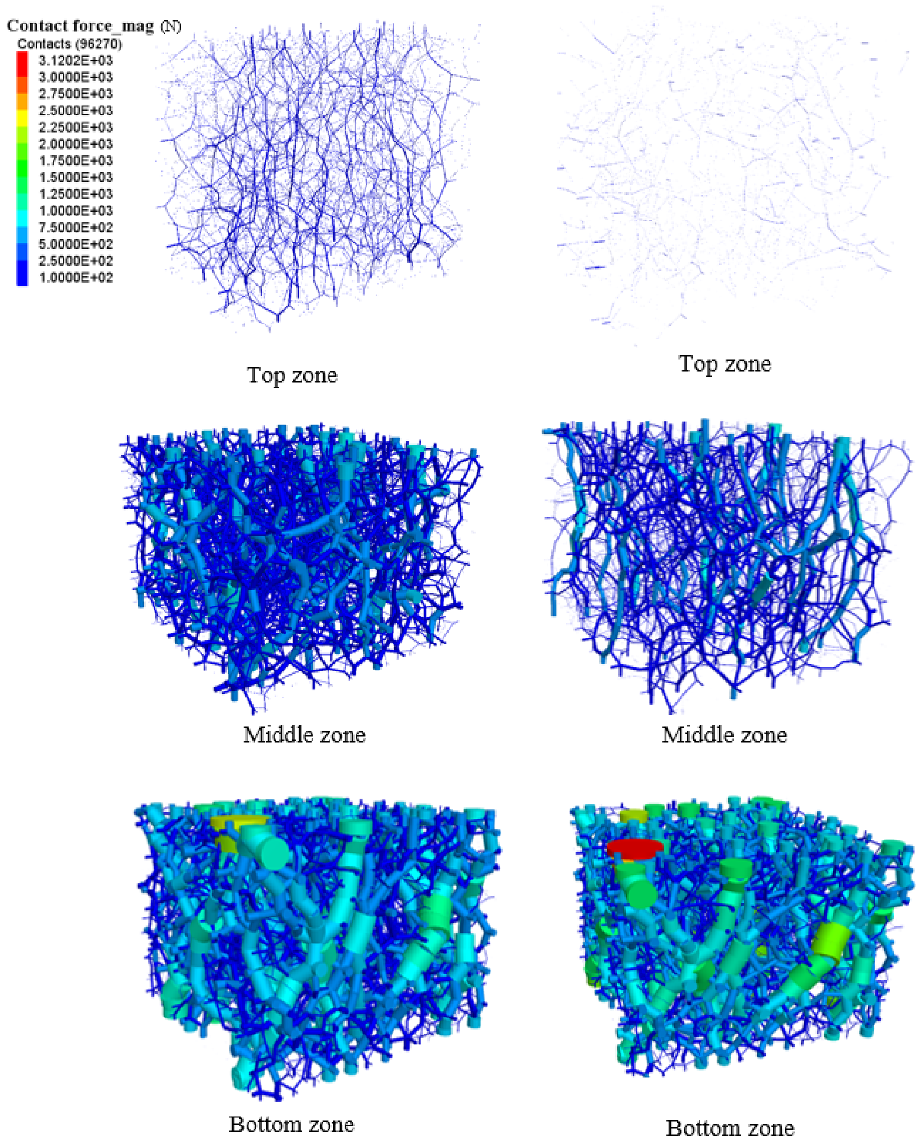

(a) T = 0 s (b) T = 10 s

Figure 23: Force networks for different zones before and after the seismic event for the loose soil column.

artificially dissipate energy similar to the Rayleigh damping, which is employed in conjunction with the case of the continuum constitutive model P2PSand. By construction, the influence of the DEM global damping parameter becomes more significant when the regime commences being far from being quasi-static, which is expected to occur during such a dynamic event and the present section investigates in detail this influence for the present multi-scale simulations.

A numerical simulation is performed for the loose soil column by using different DEM global damping coefficient values of 0.2 and 0 instead of the value of 0.6 that was employed during the previous simulations in Section 5.1 and the results are shown in Fig 24 and Fig 25. The simulation results demonstrate how the damping parameter affects the response at different levels of the column, whereby for the case of a damping value of 0.2 the top, middle and bottom zones final axial strain values increase by approximately 100%.

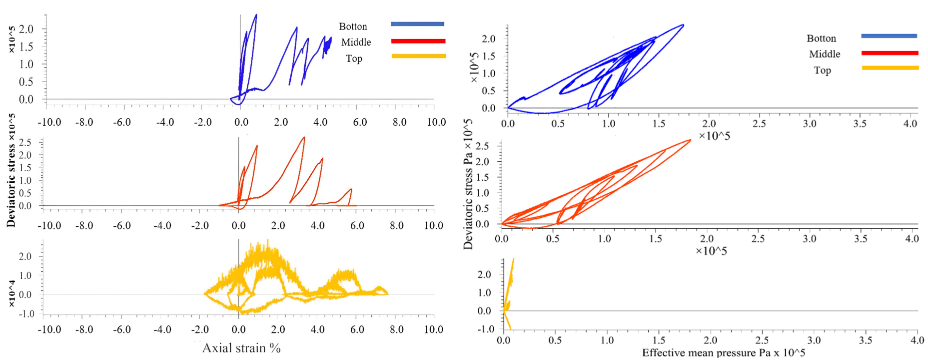

Figure 24: Multi-scale model predictions for a loose soil column $D_r = 25\%$ using global damping coefficient = 0.2.

Fig 25 also compares the effective mean pressure values for the three damping values at the end of the seismic event. Obviously, the damping parameter affects the distribution of the effective mean pressure and therefore, the liquefied zones throughout the soil column.

It is instructive at this point to study the effect of particle sizes in the DEM model (REV) during such dynamic events. The investigation is performed by using the two models in Fig. 6 in which only the particle size is changed while

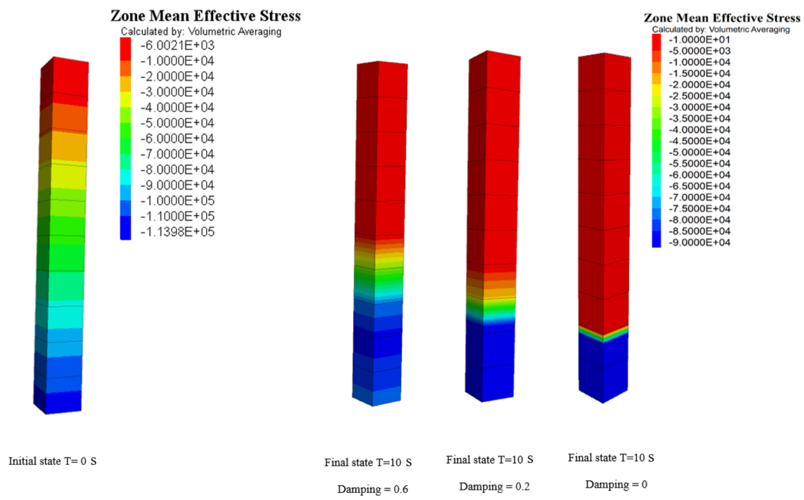

Figure 25: Initial and final values of the effective mean pressure (in Pa) through the column for different damping values for the loose case.

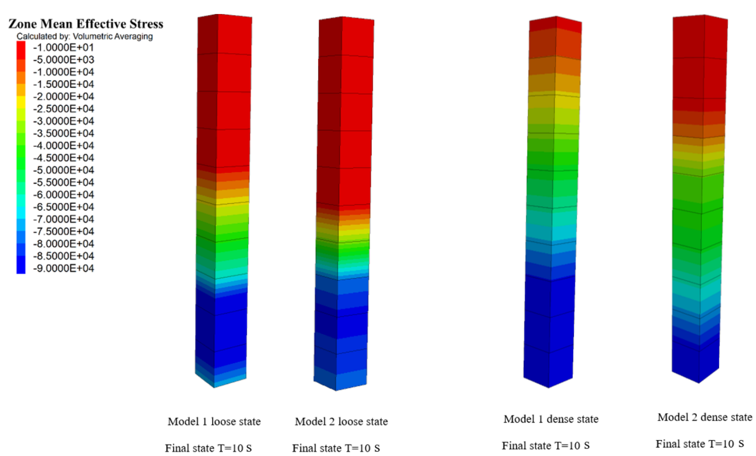

Figure 26: The final values of the effective mean pressure (in Pa) through the soil column for different particle size distributions for the loose (leftmost) and the dense (rightmost) cases and two different size distributions (gravel-like model 1 and sand-like model 2).

maintaining the same contact model, particle number, and damping coefficient. The particle size distribution of model 1 could represent a gravel-filled soil column. The results in Fig. 26 show an influence of the particle size on the distribution of the effective mean pressure along the column, indicating that soils with larger particles have less liquefaction potential due to their inertial effect. As a matter of fact, a smaller grain size (or a lower inertial number from a collisional I in the order of 10^{-2} to values around 10^{-3}, see later Fig. 29) leads to an increase in reached strains as shown in Fig. 27 and Fig. 28, consistently to previous Section 3.5.

The inertial number is evaluated to examine the dynamic effect on the previous simulations. Fig. 29 illustrates the evolution of the inertial number of the top and the bottom zones for the loose case with a damping value = 0.6. For model 1 the values of the inertial number indicate some dynamic effect on the behavior of the top zone and bottom zone coherently with the previous discussion in Section 3.5. Whereas the results of model 2 show only an intermittent dynamic effect for the top zone at different stages during the event, which can be attributed to lower effective mean pressure values and higher strain rate due to the occurrence of the liquefaction. Thus, we recall that one of the main advantages of DEM over constitutive models is its ability to consider the real physics of granular materials by taking particle inertia into account during dynamic simulations.

These inertial effects would combine in reality with another advantage of gravel-like soils against sand soils through their higher hydraulic conductivity "permeability" leading to dissipate faster pore pressure (which is not computed in the present simulation).

5.3. Discussion about the advantages and limitations of P2PSand and spherical DEM-based multiscale approaches

From the multi-scale model results in Fig. 16 and Fig. 17, it can be deduced that when an unloading path is imposed after a dilatation behavior (evolution on the failure envelope in an undrained condition), more plastic deformation and pore pressure are generated resulting in a significant decrease in

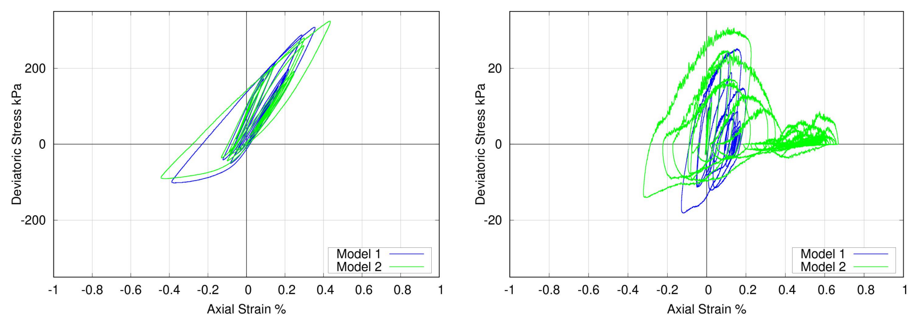

(a) Bottom zone $D_r = 60\%$ (b) Top zone $D_r = 60\%$

Figure 27: Effect of particle size on the response of the dense soil column for the bottom and top zones with a damping value = 0.6.

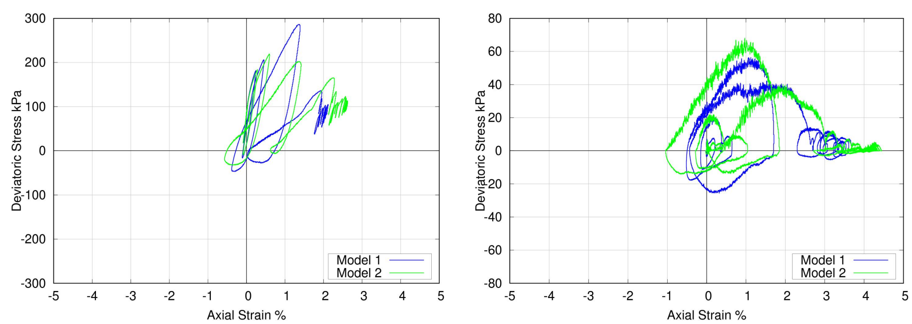

(a) Bottom zone $D_r = 25\%$ (b) Top zone $D_r = 25\%$

Figure 28: Effect of particle size of the response on the loose soil column for the bottom and top zones with a damping value = 0.6.

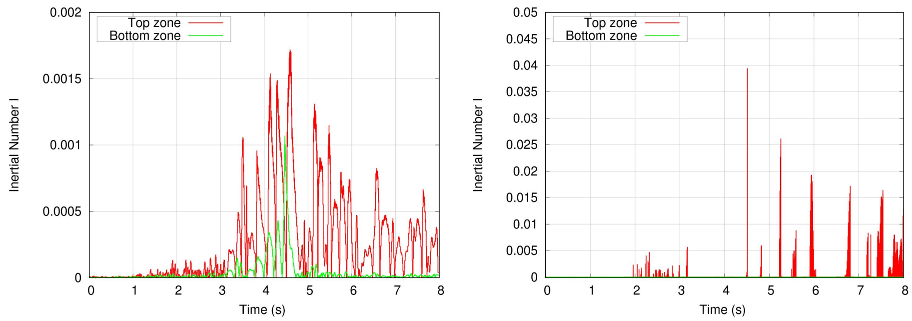

(a) Gravel-like model 1

(b) Sand-like model 2

Figure 29: The evolution of the inertial number for the bottom and top zones in the case of damping = 0.6 for D_r = 25% and different particle sizes.

effective mean pressure and deviatoric stress. However, despite the fact that the P2PSand model incorporates the influence of fabric evolution (noting that fabric anisotropy develops only when the dilatancy occurs) on the dilatancy behavior, the results of the P2PSand model contradict the DEM results at this point (which is more pronounced for the dense state, see $q - p'$ curves in Fig. 16 and Fig. 17). These results recommend calibrating the fabric parameters of the P2PSand model on cyclic triaxial for dense samples with dilative behavior. Also, they suggest to revisit the P2PSand model formulation for the stiffness-dilatancy degradation law.

On the other hand, the multi-scale approach provided an adequate seismic response by using four contact parameters (which could be reduced to three parameters in the case of a more realistic particle shape, as illustrated by Mohamed et al. (2022)) and excluded all nonphysical responses that occurred when constitutive models were used, as previously discussed. However, difficulties still remain when attempting to reproduce high-precision qualitative results for cyclic triaxial undrained tests as shown previously in Section 3.3 due to switching between triaxial compression and triaxial extension at each cycle, which can be attributed to the use of spherical particles and the lack of initial fabric consideration. Also, as highlighted by Mohamed et al. (2022) (Figs. 18-19 therein), although the spherical shapes together with the rolling resistance contact model can provide a good agreement with the experimental triaxial tests, irregular shapes still better match the experimental data in terms of the initial slope in the $q - \epsilon_a$ curve, volumetric contraction behavior and stress softening behavior.

One should additionally consider the small strain properties of soil (Hardin and Richart Jr, 1963; Tatsuoka et al., 1979), i.e. the small-strain modulus G_{max} because of its important role in wave propagation mechanisms and liquefaction potential. Fig. 30 shows the prediction of the DEM model for the relation $G_{max} - p'$ estimated from undrained triaxial tests at 10^{-5} strain amplitude together with experimental data by Tatsuoka et al. (1979). While the DEM results are of the correct order of magnitude, with just a 26% discrepancy for the smallest confining pressures considered in the study (50 kPa), they also confirm that the linear rolling resistance contact model used in this study in conjunction with spherical particles cannot offer the expected mean pressure dependency of small-strain modulus G_{max} on the effective mean pressure p' (as adopted in the P2PSand model in Eq. A.5). Therefore, a more adequate contact formulation could improve the DEM REV behavior in this aspect, such as the Hertz model (Itasca, 2018; Mindlin and Deresiewicz, 1953) or a more advanced contact model as adopted by Kuhn (2022).

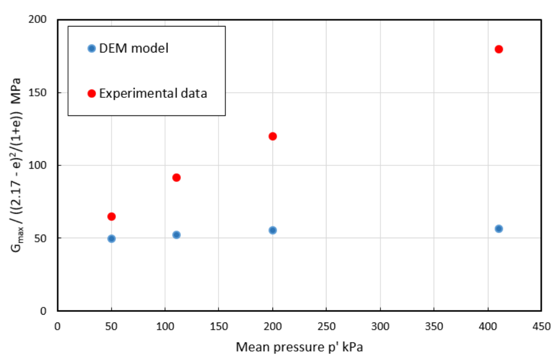

Figure 30: Comparison between the DEM model (initial void ratio = 0.63) and experimental data from Tatsuoka et al. (1979) for the relationship between small-strain modulus G_{max} and mean pressure p' for Toyoura sand.

As another important issue, the spherical model has a strong tendency to show isotropy (as it is the case after the isotropic preparation phase, Table 2), lacking inherent fabric anisotropy which would induce for instance anisotropic elastic characteristics and possibly impact seismic waves propagation.

Finally, Table 3 summarizes the different modeling choices for the multi-scale and DEM models and highlights the achievements and shortcomings of the proposed approach.

Table 3: Commented summary of the different modelling choices within the multi-scale and DEM models.

Modelling topic	Chosen approach	Remark
	Proposed multi-scale approach	
Coupling Scheme	FVM-DEM FLAC3D-PFC	No need for a tangent stiffness matrix Less computational time
Stress matrix expression	Inclusion of inertial effects in DEM	Appropriate for seismic and dynamic simulations
Hydro-mechanical coupling	Inclusion of mechanically-induced pore pressure evolution	Darcy's law not activated herein
	Used DEM model	
Particles shape	Spherical	10 - 100 times faster computational time (Mohamed et al., 2022; Duriez and Bonelli, 2021)
Contact model	Rolling resistance model with constant stiffness	Not able to reproduce $G_{max} - p'$ curve
Packing and its preparation	Isotropic packing with 7000 particles	Appropriate REV is achieved Lack of inherent anisotropy
Calibration and validation at lab-scale	Calibration on monotonic and cyclic tests while using same void ratio as experiments	Very good prediction for monotonic loading Less precise prediction for cyclic tests

5.4. Computational time and software parallelization aspects

In terms of computational time, executing the FLAC3D-PFC multi-scale model is logically significantly longer than a pure FLAC3D simulation: 6 hours vs 20 minutes for the current study respectively, as obtained utilizing a workstation with 8 cores, 3.0 GHz CPU and 64 GB RAM. Since differences in operations reduce to the application of the DEM or P2PSand models as a constitutive relation, it is evident that the majority of the time cost for the multi-scale coupling comes from PFC-DEM computations. The amount of the latters is directly proportional to the number of zones, with evident higher costs to be expected for more complex BVP in terms of mesh than the one considered here. On the other hand, the present choice of studying a 1D wave propagation is not computationally important in itself and 2D or 3D propagation studies with a similar number of zones, if possible, would show the same time requirements.

In order to alleviate DEM-induced time costs, one should note that PFC supports parallel DEM simulations by distributing the computational load on the available cores allowing multi-threaded computation for contact detection and contact model with an efficient spatial searching and contact detection scheme.

It could also be thought of to apply parallelization to FLAC3D structure-scale operations with simultaneous computations of DEM REVs, as discussed e.g. by Kuhn (2022).

6. Concluding summary and perspectives

This paper compares a discrete-based approach and one advanced bounding surface plasticity model 'P2PSand' for sand behavior and the propagation of seismic waves after a fair calibration and validation procedure of the two approaches on lab experiments. A 3D multi-scale FVM×DEM scheme is established between a continuum code Flac3D and discrete element PFC code to solve boundary value problems by using the DEM as a constitutive model.

Thanks to its use of the common and well-documented FLAC3D-PFC codes, as well as the ingredients of the coupling scheme (e.g., inertial effect), the proposed model can be used within various complex 3D numerical simulations for soils, including cyclic and shock loading. Also, the implementation of the present multi-scale scheme is less complex than the FEM×DEM scheme found in the literature since in the explicit FVM×DEM scheme there is no need to establish a consistent tangent stiffness matrix from the macroscopic computation, which can reduce the computational time of simulations. Numerical results demonstrate the accuracy of the implemented coupling scheme through classical stress paths applied on one or two zones. On the other hand, proper implementation and application of the averaged stress tensor calculated from the DEM part require careful treatment. The inertial term in the homogenization formula of stress for granular assembly is shown to be an essential term during dynamic simulations with higher inertial number values, such as severe earthquakes and impact loadings. It is found that by increasing the inertial number, the strength of the granular material increases, accompanied by more dilative behavior and no clear critical state condition.

The DEM and P2PSand models have been calibrated and validated based on experimental laboratory data of Toyoura sand for monotonic and cyclic loadings. The validated DEM model is used via multi-scale modeling to analyze the wave propagation mechanism in a saturated soil column made of Toyoura sand and is compared with the predictions of the P2PSand model. Results reveal several differences in response evolution logic between the two models. First, the so-called butterfly loops in the effective stress plane and the hysteretic loops in the deviatoric axial strain plane are quite different for the two models under dense and loose cases. Second, for dense and loose conditions, the P2PSand model accumulates more axial strain than the multi-scale model, resulting in a possible underestimation of the resistance of any earth structure under cyclic loadings.

In addition, the parametric study performed on the effect of the DEM numerical damping coefficient highlighted the importance of this parameter during seismic or dynamic events. Results of the propagation of seismic waves show that different damping values can affect the final distribution of pore pressure as well as the final deformation of the column. In such a case, minimizing the DEM global damping parameter is essential to ensure more realistic results and avoid an artificial decrease in strain estimations that would be detrimental to structural stability in engineering studies. As for the particle size effect, it is found that the two models with different particle size distributions are influenced by some dynamic effect in different ways. First, for the model that has the same size as Toyoura sand, the behavior was quasi-static during the first stage of the event, however, when liquefaction occurred at some positions in the soil column, the behavior became more dynamic due to the low value of the effective mean pressure. As for the case with larger particle size, the simulations are shown to be dynamic by tracking the values of the inertial number which indicates that soils with larger particles have a greater dynamic contribution to stress that leads to less liquefaction potential.

Finally, the computational time for the multi-scale model is significantly longer, taking six hours compared to a 20-minute simulation in the case of the P2PSand model. However, considering the precision of the multi-scale method, this computational time is quite acceptable.

Further perspective for this work is to investigate cyclic behavior and multi-scale modeling of the behavior of the polyhedron DEM model also presented in (Mohamed et al., 2022) since the latter is more realistic, e.g., for what concerns initial fabric consideration (material inherent anisotropy) than the present spherical model. First, to verify to what extent the initial fabric consideration could improve the cyclic behavior and cyclic mobility of a DEM model compared to experimental data. Second, to quantify its influence on the final values of strain and effective mean pressure for boundary value problems, e.g., comparison between the polyhedron and sphere DEM models for the previous example of seismic wave propagation. In addition, we intend to use the present multi-scale scheme for modeling the seismic behavior of a real earth dam.

Acknowledgements

The authors would like to express their sincere thanks and gratitude to the Itasca Educational Partnership Program (IEP, Zhao Cheng and Sacha Emam) for their valuable support and for providing PFC software, to SUEZ-SAFEGE for the funding of the Ph.D. associated with this article. The authors would like to particularly thank Prof. Gaël Combe (Grenoble Alps University, France) for discussing and providing valuable feedback regarding the multi-scale modeling. The authors are also grateful to Dr. Hailong Wang (Waseda University, Japan) for providing raw experimental data.

Appendix A. P2PSand Constitutive formulas

A power relationship relating here the critical relative density D_{rc} to p' across different ranges of the confining pressures:

$$D_{rc} = D_{rc0} + \lambda_c \left(\frac{p'}{p_{atm}}\right)^{\zeta} \tag{A.1}$$

Where λ_c, ζ and D_{rc0} are three positive model parameters.

$$I_p = \frac{p'}{p_c} \tag{A.2}$$

Eq. (A.1) is complemented in the (deviatoric) stress space by a critical state surface giving the $M = \sqrt{3/2}||\boldsymbol{s}||/p$ ratio at the critical state, M^c for any Lode angle θ, from its critical values during triaxial compression and triaxial extension. Denoting the latters M_{comp} and M_{ext} respectively and $c = M_{ext}/M_{comp}$ the corresponding ratio as a model parameter, the same Lode angle dependency than Cheng and Detournay (2021) is considered:

$$\frac{M^c(\theta)}{M_{comp}} = g(\theta, c) = \left(\frac{2c^4}{c^4 + 1 + (c^4 - 1)\cos 3\theta}\right)^{0.25} \tag{A.3}$$

The critical-strength parameter M_{comp} may be expressed in the form of a Mohr-Coulomb friction angle for the same triaxial compression path, ϕ_{comp}.

At the other end of the behavior, for small deformations, the incremental form of the elastic part is defined as follows:

$$dp' = -Kd\epsilon_v^e \qquad d\boldsymbol{s} = 2Gd\boldsymbol{e}^e \tag{A.4}$$

Where p' is the effective mean stress (isotropic stress) and $\boldsymbol{s}$ is the deviatoric stress tensor. K and G are bulk and shear modulus respectively. ϵ_v and $\boldsymbol{e}$ are volumetric strain and deviatoric strain tensor respectively. The P2PSand hypoelastic law is adopted for expressing K and G as a function of the current relative density and the current mean effective pressure :

$$G = G_0(D_r + C_{Dr})p_{atm}\left(\frac{p'}{p_{atm}}\right)^n \qquad K = \frac{2(1+\nu)}{3(1-2\nu)}G \tag{A.5}$$

The model proposes a power law for the bounding and dilatancy surfaces. The form of these surfaces is the same as the critical state surface and has an additional dependency on the relative state index I_p and relative density D_r as follows:

$$M^d(\theta) = M^c(\theta) I_p^{(n_d D_r)} \qquad M^b(\theta) = M^c(\theta) I_p^{(-n_b D_r)} \tag{A.6}$$

where $M^d(\theta)$ and $M^b(\theta)$ denote dilatancy and bounding surfaces respectively. Finally, the images of the kinematic hardening tensor $\boldsymbol{\alpha}$ on the dilatancy and bounding surfaces are defined as the intersection points between a parallel line to the loading direction $\boldsymbol{n}$ stemming from the origin point to the dilatancy or bounding surfaces as shown in Fig. 1. $\boldsymbol{n}$ is the loading direction tensor outward along the radius $\boldsymbol{r}$ - $\boldsymbol{\alpha}$ and is defined as:

$$\boldsymbol{n} = \frac{\boldsymbol{s} - p'\boldsymbol{\alpha}}{||\boldsymbol{s} - p'\boldsymbol{\alpha}||} \tag{A.7}$$

The image tensors on the different surfaces can be expressed as follows:

$$\boldsymbol{\alpha}_\theta^{d,b,c} = \sqrt{2/3}[g(\theta, c)M^{d,b,c} - m]\boldsymbol{n} \tag{A.8}$$

The plastic volumetric strain can be related to dilatancy as follows:

$$d\epsilon_v^p =< L > D \tag{A.9}$$

For virginal loading, the dilatancy is defined based on the distance between the current $\boldsymbol{\alpha}$ and its image on the dilatancy surface $\boldsymbol{\alpha}_\theta^d$ as proposed by Dafalias and Manzari (2004).

$$D = A_d(\boldsymbol{\alpha}_\theta^d - \boldsymbol{\alpha}) : \boldsymbol{n} \tag{A.10}$$

where A_d is a model variable that depends on the fabric state and will be defined later. If the state of $\boldsymbol{\alpha}$ is inside the MBS, a new term will be added to the dilatancy equation to avoid the overshooting of the dilatancy during cyclic loading as follows:

$$D_{Cyc} = A_{d0}(\boldsymbol{\alpha}_\theta^d - \alpha) : \boldsymbol{n} * k_{Cyc}(\boldsymbol{\alpha} - \boldsymbol{\alpha}_{in}) : \boldsymbol{n} \tag{A.11}$$

where k_{cyc} is a calibration parameter for cyclic loading. In the present model fabric tensor dz evolution is described as follows:

$$d\boldsymbol{z} = - < L > c_z(\sqrt{\frac{2}{3}} z_{max}\boldsymbol{n} + z), D > 0 \tag{A.12}$$

The fabric tensor $\boldsymbol{z}$ evolves only during dilatancy dilation. Finally, dilatancy is impacted by the fabric evolution as follows:

$$A_d = A_{d0}(1 + \sqrt{\frac{2}{3}} < \boldsymbol{z} : \boldsymbol{n} >) \tag{A.13}$$

Appendix B. Flac3D continuum equations

The momentum principle of motion (Cauchy's equations) is:

$$\sigma_{ij,j} + \rho b_i = \rho \frac{dv_i}{dt} \tag{B.1}$$

For a body in equilibrium or steady state Eq. B.1 is reduced to :

$$\sigma_{ij,j} + \rho b_i = 0 \tag{B.2}$$

In Flac3D, the equation of motion is applied to the mesh nodes. To this end, the finite volume approximation of the space derivative is applied to obtain a description of the strain rate tensor as a function of nodal velocities by assuming that the velocity field varies linearly inside the tetrahedron. The Gauss divergence theorem to the tetrahedron relates the divergence of the velocity field inside a volume V and the flux through a surface S as follows:

$$\int_V v_{i,j} dV = \int_S v_i n_j dS \tag{B.3}$$

where $v_{i,j}$ is the gradient of the velocity field and n_j is the normal to the surface. The infinitesimal strain rate tensor is defined as:

$$\dot{\epsilon_{ij}} = \frac{1}{2}(v_{i,j} + v_{j,i}) \tag{B.4}$$

The average velocity of each face of tetrahedron $\overline{v_i}^{(f)}$ can be defined from their nodal velocities as follows :

$$\overline{v_i}^{(f)} = \frac{1}{3} \sum_{l=1, l\neq f}^{4} v_i^l \tag{B.5}$$

where the superscript l represents the nodal number. From Eq. B.3, the strain rate tensor in Eq. B.4 and Eq. B.5 can easily define the relation between strain rate tensor and nodal velocities.

$$\dot{\epsilon_{ij}} = \frac{1}{6V} \sum_{l=1}^{4} \left(v_i^l \; n_j^{(l)} + v_j^l \; n_i^{(l)} \right) \; S^{(l)} \tag{B.6}$$

The final goal is to apply the equation of motion to the different nodes by using an explicit finite difference approximation to the time derivative. In order to obtain the nodal formulation of the equation of motion, the concept of virtual work is applied to a tetrahedron by multiplying the net force in Eq. B.1 by an imaginary velocity applied at the tetrahedron centroid as follows:

$$\delta P = (\sigma_{ij,j} + \rho b_i - \rho \frac{dv_i}{dt}).\delta v_i = 0 \tag{B.7}$$

where P is the power. Since the velocity varies linearly inside the tetrahedron, dv_i can be expressed as a function of nodal velocity as follows:

$$\delta \; v_i = \frac{1}{4} \sum_{n=1}^{4} \delta \; v_i^n \tag{B.8}$$

The internal power can be expressed as a function of nodal velocities and the nodal force vector T_i^l (from Cauchy's formula) as follows:

$$T_i^l = \sigma_{ij} \; n_j^{(l)} \; S^{(l)} \tag{B.9}$$

$$P^{Internal} = -\frac{1}{3} \sum_{l=1}^{4} \delta \; v_i^l \; T_i^l \tag{B.10}$$

In turn, the external power done by the body force and inertial force is expressed as follows:

$$P^{External} = \sum_{n=1}^{4} \delta \; v_i^n [\frac{\rho \; b_i \; V}{4} - \frac{\rho \; V}{4} (\frac{dv_i}{dt})^l] \tag{B.11}$$

where $\frac{\rho \; V}{4}$ is the nodal mass m^l. From Eq. B.11 and Eq. B.10, the nodal formulation of the equation of motion can be expressed as:

$$m^l (\frac{dv_i}{dt})^l = \frac{T_i^l}{3} + m^l b_i + P_i^l = F_i^l \tag{B.12}$$

where F_i^l is the out-of-balance force and P_i^l is the external force applied to a node. Finally, the explicit finite difference approximation for the derivative $(\frac{dv_i}{dt})^l$ to obtain the new nodal velocity is as follows:

$$v_i^{<l>}(t + \frac{\Delta t}{2}) = v_i^{<l>}(t - \frac{\Delta t}{2}) + \frac{\Delta t}{m^{<l>}} F_i^{<l>} \tag{B.13}$$

The present multi-scale model also includes hydro-mechanical coupling as available in FLAC3D with, for the present saturated conditions:

$$\boldsymbol{\sigma}' = \boldsymbol{\sigma} - p\boldsymbol{I} \tag{B.14}$$

$$\frac{1}{M}\frac{\partial p}{\partial t} = -q_{i,i} + q_v - \alpha_{Biot}\frac{\partial \epsilon}{\partial t} \tag{B.15}$$

Where $\boldsymbol{\sigma}'$ is effective stress and $\boldsymbol{I}$ is the Kronecker tensor. $\frac{\partial p}{\partial t}$ is the variation of pore pressure with respect to the time, M is the Biot modulus ($= k_f$ here), α_{Biot} is the Biot coefficient ($= 1$ here) and ϵ is the mechanical volumetric strain. q_i is the specific discharge vector described by Darcy's law $q_i = -k_i \nabla p$ (k_i and ∇p are mobility coefficients matrix and pressure head gradient) and q_v is the volumetric fluid source intensity respectively. These last two terms are disregarded here even though they could be included by activating fluid flow option in FLAC3D.

References

Bagi, K., 2003. Discussion on "the asymmetry of stress in granular media" by jp bardet and i. vardoulakis:[int. j. solids and structures, vol. 38, pp. 353–367 (2001)]. International Journal of Solids and Structures 40, 1329–1331.

Been, K., Jefferies, M.G., 1985. A state parameter for sands. Géotechnique 35, 99–112.

Byrne, P.M., 1991. A cyclic shear-volume coupling and pore pressure model for sand. in Proceedings: Second International Conference on Recent Advances in Geotechnical Earthquake Engineering and Soil Dynamics (St. Louis, Missouri, March 1991) Paper No. 1.24, 47–55.

Cappellaro, C., Cubrinovski, M., Bray, J.D., Chiaro, G., Riemer, M.F., Stringer, M.E., 2021. Liquefaction resistance of christchurch sandy soils from direct simple shear tests. Soil Dynamics and Earthquake Engineering 141, 106489.

Cheng, Z., Detournay, C., 2021. Formulation, validation and application of a practice-oriented two-surface plasticity sand model. Computers and Geotechnics 132, 103984.

Christoffersen, J., Mehrabadi, M.M., Nemat-Nasser, S., 1981. A micromechanical description of granular material behavior. Journal of Applied Mechanics 48, 873–885. doi:10.1115/1.3157619.

Cundall, P.A., 1987. Distinct element models of rock and soil structure. Analytical and computational methods in engineering rock mechanics , 129–163.

Da Cruz, F., Emam, S., Prochnow, M., Roux, J.N., Chevoir, F., 2005. Rheophysics of dense granular materials: Discrete simulation of plane shear flows. Physical Review E 72, 021309.

Dafalias, Y.F., Manzari, M.T., 2004. Simple plasticity sand model accounting for fabric change effects. Journal of Engineering mechanics 130, 622–634.

Dafalias, Y.F., Papadimitriou, A.G., Li, X.S., 2004. Sand plasticity model accounting for inherent fabric anisotropy. Journal of Engineering Mechanics 130, 1319–1333.

De Saxcé, G., Fortin, J., Millet, O., 2004. About the numerical simulation of the dynamics of granular media and the definition of the mean stress tensor. Mechanics of Materials 36, 1175–1184.

Dong, Q., Xu, C., Cai, Y., Juang, H., Wang, J., Yang, Z., Gu, C., 2016. Drained instability in loose granular material. International Journal of Geomechanics 16, 04015043.

Duriez, J., Bonelli, S., 2021. Precision and computational costs of Level Set-Discrete Element Method (LS-DEM) with respect to DEM. Computers and Geotechnics 134, 104033. doi:10.1016/j.compgeo.2021.104033.

Duriez, J., Darve, F., Donze, F.V., 2011. A discrete modeling-based constitutive relation for infilled rock joints. International journal of rock mechanics and mining sciences 48, 458–468.

Duriez, J., Vincens, É., 2015. Constitutive modelling of cohesionless soils and interfaces with various internal states: An elasto-plastic approach. Computers and Geotechnics 63, 33–45.

Duriez, J., Wan, R., 2017. Subtleties in discrete-element modelling of wet granular soils. Géotechnique 67, 365–370.

Fukushima, S., Tatsuoka, F., 1984. Strength and deformation characteristics of saturated sand at extremely low pressures. Soils and Foundations 24, 30–48.

Gu, X., Zhang, J., Huang, X., 2020. Dem analysis of monotonic and cyclic behaviors of sand based on critical state soil mechanics framework. Computers and Geotechnics 128, 103787.

Guo, N., Zhao, J., 2014. A coupled fem/dem approach for hierarchical multiscale modelling of granular media. International Journal for Numerical Methods in Engineering 99, 789–818.

Hardin, B.O., Richart Jr, F., 1963. Elastic wave velocities in granular soils. Journal of the Soil Mechanics and Foundations Division 89, 33–65.

Itasca, 2018. Pfc — particle flow code, ver. 6.0. Itasca Consulting Group, Inc.

Itasca, 2019. Flac3d - fast lagrangian analysis of continua in three dimensions, version 7.0. Itasca Consulting Group, Inc.

Jop, P., Forterre, Y., Pouliquen, O., 2006. A constitutive law for dense granular flows. Nature 441, 727–730.

Kouznetsova, V., Geers, M.G., Brekelmans, W.M., 2002. Multi-scale constitutive modelling of heterogeneous materials with a gradient-enhanced computational homogenization scheme. International journal for numerical methods in engineering 54, 1235–1260.

Kuhn, M.R., 2022. Multi-scale simulation of wave propagation and liquefaction in a one-dimensional soil column: hybrid dem and finite-difference procedure. Acta Geotechnica 17, 2611–2632.

Kuhn, M.R., Daouadji, A., 2020. Simulation of undrained quasi-saturated soil with pore pressure measurements using a discrete element (dem) algorithm. Soils and Foundations 60, 1097–1111.

Kutter, B.L., Manzari, M.T., Zeghal, M., 2019. Model tests and numerical simulations of liquefaction and lateral spreading: LEAP-UCD-2017. Springer Nature.

Li, X.S., Wang, Y., 1998. Linear representation of steady-state line for sand. Journal of geotechnical and geoenvironmental engineering 124, 1215–1217.

Liu, Y., Sun, W., Yuan, Z., Fish, J., 2016. A nonlocal multiscale discrete-continuum model for predicting mechanical behavior of granular materials. International Journal for Numerical Methods in Engineering 106, 129–160.

Martin, G.R., Seed, H.B., Finn, W.L., 1975. Fundamentals of liquefaction under cyclic loading. Journal of the Geotechnical Engineering Division 101, 423–438.

Mindlin, R.D., Deresiewicz, H., 1953. Elastic spheres in contact under varying oblique forces .

Mohamed, T., Duriez, J., Veylon, G., Peyras, L., 2022. DEM models using direct and indirect shape descriptions for toyoura sand along monotonous loading paths. Computers and Geotechnics 142, 104551. doi:10.1016/j.compgeo.2021.104551.

Nguyen, T.K., Claramunt, A.A., Caillerie, D., Combe, G., Dal Pont, S., Desrues, J., Richefeu, V., 2017. Fem× dem: a new efficient multi-scale approach for geotechnical problems with strain localization, in: EPJ Web of Conferences, EDP Sciences. p. 11007.

Nguyen, T.K., Combe, G., Caillerie, D., Desrues, J., 2014. Fem× dem modelling of cohesive granular materials: numerical homogenisation and multi-scale simulations. Acta Geophysica 62, 1109–1126.

Nitka, M., Bilbie, G., Combe, G., Dascalu, C., Desrues, J., 2009. A dem—fem two scale approach of the behaviour of granular materials, in: AIP Conference Proceedings, American Institute of Physics. pp. 443–446.

Roscoe, K.H., Burland, J.B., 1968. On the generalized stress-strain behavior of wet clays, in: Engineering plasticity, pp. 535–609.

Sibille, L., Villard, P., Darve, F., Aboul Hosn, R., 2019. Quantitative prediction of discrete element models on complex loading paths. International Journal for Numerical and Analytical Methods in Geomechanics 43, 858–887.

Taiebat, M., Jeremić, B., Dafalias, Y.F., Kaynia, A.M., Cheng, Z., 2010. Propagation of seismic waves through liquefied soils. Soil Dynamics and Earthquake Engineering 30, 236–257.

Tatsuoka, F., Iwasaki, T., Yoshida, S., Fukushima, S., Sudo, H., 1979. Shear modulus and damping by drained tests on clean sand specimens reconstituted by various methods. Soils and Foundations 19, 39–54.

Tsiaousi, D., Ugalde, J., Travasarou, T., 2020. Leap-ucd-2017 simulation team fugro, in: Model Tests and Numerical Simulations of Liquefaction and Lateral Spreading: LEAP-UCD-2017, Springer. pp. 545–562.

Wang, H., Koseki, J., Sato, T., Chiaro, G., Tian, J.T., 2016. Effect of saturation on liquefaction resistance of iron ore fines and two sandy soils. Soils and Foundations 56, 732–744.

Weber, J., 1966. Recherches concernant les contraintes intergranulaires dans les milieux pulvérulents. Bulletin de liaison des Ponts et Chaussées 20, 1–20.

Woodward, P., Griffiths, D., 1996. Influence of viscous damping in the dynamic analysis of an earth dam using simple constitutive models. Computers and Geotechnics 19, 245–263.

Xie, X., Ye, B., Zhao, T., Feng, X., Zhang, F., 2022. Effects of prior non-liquefying undrained cyclic loading on sand liquefaction resistance via discrete element analysis. Soil Dynamics and Earthquake Engineering 161, 107390.

Yan, B., Regueiro, R.A., 2019. Definition and symmetry of averaged stress tensor in granular media and its 3d dem inspection under static and dynamic conditions. International Journal of Solids and Structures 161, 243–266.

Yang, M., Barrero, A.R., Taiebat, M., 2020. Application of a sanisand model for numerical simulations of the leap 2017 experiments, in: Model Tests and Numerical Simulations of Liquefaction and Lateral Spreading: LEAP-UCD-2017, Springer. pp. 595–610.

Yoshimine, M., 2013. Yoshimine m. archives – soil mechanics laboratory. Tokyo Metro-politan.

Yoshimine, M., Robertson, P., Wride, C., 1999. Undrained shear strength of clean sands to trigger flow liquefaction. Canadian Geotechnical Journal 36, 891–906.